Analysis and modelling of longitudinal deformation profiles of tunnels excavated in strain-softening time-dependent rock masses

Fei Song[1], Alfonso Rodriguez-Dono[1,2]*, Sebastia Olivella[1], Zhen Zhong[3,4]

1 Department of Civil and Environmental Engineering,

Technical University of Catalonia (UPC), Spain, 08034

2 Institute of Environmental Assessment and Water Research (IDAEA),

Spanish National Research Council (CSIC), Spain, 08034

3 Key Laboratory of Rock Mechanics and Geohazards of Zhejiang Province,

Shaoxing University, China, 312000

4 College of Civil Engineering,

Shaoxing University, China, 312000

* Corresponding author: Alfonso Rodriguez-Dono

E-mail address: alfonso.rodriguez@upc.edu

Abstract

Rock mass behaviour model selection, in particular, to represent the post-failure behaviour and time-dependent behaviour of rock masses, are critical issues in the correct application of tunnelling design techniques such as the convergence-confinement method or numerical modelling. This study provides a general numerical approach for predicting longitudinal deformation profiles using a coupled ViscoElastic-ViscoPlastic Strain-Softening (VEVP-SS) model. A viscous dashpot and the strain-softening model are coupled to simulate the progressive damage process and creep failure behaviour of rock masses. Different failure criteria are considered to simulate the post-failure behaviour. As a verification step, numerical creep tests are carried out to analyse the coupled behaviour, and the basic viscoelastic and strain-softening results of the VEVP-SS model are compared with analytical solutions and numerical results. The proposed method is able to consider the coupling between post-failure behaviour and time-dependent behaviour, thus providing a new alternative method for preliminary tunnel design. Parametric analyses are then carried out to investigate the influence of different aspects on the longitudinal deformation profiles. The tunnel deformation based on the VEVP-SS model is larger than the corresponding elastic-plastic results due to the contribution of the creep behaviour, and the excavation rate becomes relevant when considering time-dependent behaviour.

Keywords: post-failure behaviour, time-dependent behaviour, creep, tunnelling, longitudinal deformation profiles, CODE_BRIGHT

1. Introduction

In a geomechanics framework, accidents are frequently related to fractures. The complexity of different geomaterials makes the study of these fractures a critical topic for the understanding of their behaviour; such a study constitutes a very important step in the mitigation of accidents that may occur in mining or civil engineering works such as tunnel excavation [1, 2]. Rock masses undergo progressive damage and long-term viscous behaviour throughout excavation and construction. Some underground structures show large delayed displacements that could lead to failure [3]. The effect of time on rock mass deformability and strength is a topic of considerable interest in rock mechanics [4, 5]. Therefore, a proper selection of rock mass behaviour models and a proper simulation of the entire process of excavation and construction are crucial to obtain a reliable tool to achieve the optimal design of tunnels.

Most tunnel designs are currently based on empirical, analytical or numerical methods [1, 3, 6-44]. Among all these methods, the convergence-confinement method (CCM) is an analytical method that was developed in the 1930s [45] and later refined by other researchers [7, 26, 29, 32, 36, 37, 46]. It provides an efficient way to determine supporting forces by considering the rock-support interactions [26, 36]. The CCM consists of three basic components in the form of graphs:

1. The longitudinal deformation profile (LDP) relates the radial displacements of an unsupported tunnel section with its longitudinal distance to the tunnel face.

2. The ground reaction curve (GRC) establishes the relationship between the decreasing inner pressure and the increasing radial displacements of the tunnel wall.

3. The support characteristic curve (SCC) represents the stress-strain relationship of the support system [26, 29, 36]. Then, an adequate design of the required support system can be achieved by taking into account the distance from the tunnel face at which the support will be installed and the supporting forces to which the

support will be subjected, which can be obtained by the intersection of the GRC and the SCC, as shown in Figure 1.

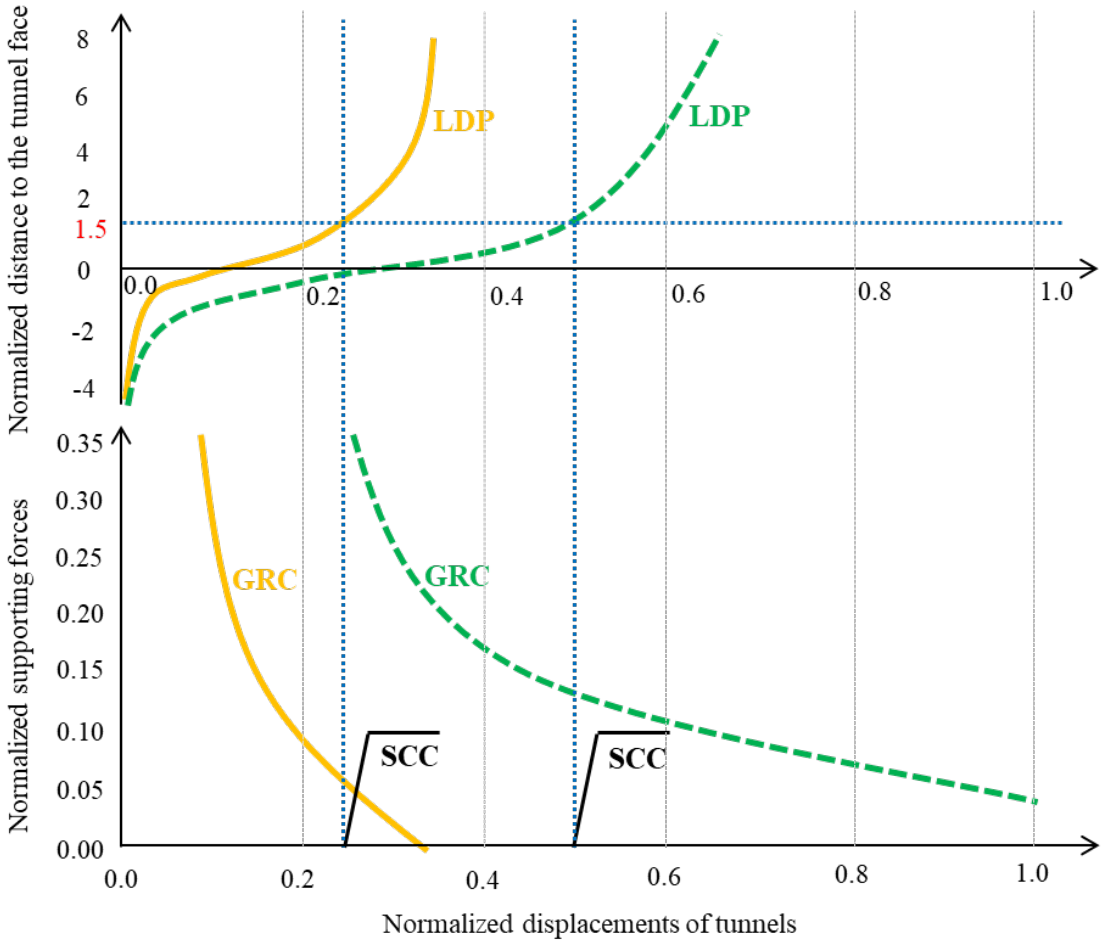

Figure 1. Main elements of the convergence-confinement method (CCM). Typical graphs obtained for the longitudinal deformation profile (LDP) above and for the ground reaction curve (GRC) and the supporting characteristic curve (SCC) below. Different lines indicate different rock mass behaviour models: elastic-perfectly plastic (EPP) in the solid yellow line and strain-softening (SS) in the slashed green line. Based on [36].

The GRC has been studied by various researchers [18, 20, 24, 28, 35, 47-49]. Hoek and Brown initially presented the SCC for different types of support structures [50], and then further research on the topic was carried out by other researchers [37, 51, 52].

However, the main focus of this article also includes the longitudinal deformation profile (LDP). Many researchers have derived solutions for the LDP, most of which are based on the elastic [46, 53-55] and elastic-perfectly plastic (EPP) behaviour of rock masses [27, 32, 37]. These models, nonetheless, do not seem to properly model the behaviour for average-quality rock masses [36, 56]. The response of rock masses will differ depending on the selected model. Considering post-failure behaviour, Alejano et al. [36] extended the Vlachopoulos and Diederichs [32] approach to the case of strain-softening rock masses, representing a wider range of rock masses, which can be used to obtain a more realistic approach to calculate the LDP. In fact, the LDP and the GRC heavily depend on the behaviour model chosen for the rock mass [36].

In Figure 1, the support design of a tunnel is estimated using CCM. If the support system is installed at a distance of 1.5 times the tunnel radius from the tunnel face, the support strength is enough to withstand the load when considering an EPP approach for the calculation of both the LDP and the GRC. However, at the same distance from the tunnel face, the support will collapse if the GRC and the LDP are calculated according to a strain-softening approach. Therefore, if the rock mass model cannot reproduce the actual behaviour of the rock mass, the resulting design may be unsafe. In the current research, a strain-softening model will be adopted to simulate the post-failure behaviour of rock masses.

Nevertheless, the solutions mentioned above do not consider the ductile properties of rock masses. Most types of rock masses exhibit significant ductile characteristics [15, 31, 57], which are known to induce gradual deformations over time that occur even after the completion of underground excavations. Some researchers presented solutions for tunnels excavated in viscoelastic geomaterials [8, 9, 21, 34], but plastic

behaviour cannot be accounted for in viscoelastic models. On the other hand, many researchers proposed elastic-viscoplastic models [11, 19, 39, 42, 58-61], three-stage creep (3SC) model [25, 42] or Stress Hardening ELastic VIscous Plastic (SHELVIP) model [25, 39] to simulate the creep and damage behaviour of geomaterials, but few of these models were used for the estimation of the LDP.

Moreover, few of these models consider a Mohr-Coulomb/Hoek-Brown strain-softening model, which may be important to model tunnel behaviour, especially in average-quality rock masses [35, 36]. Based on the Burgers-creep viscoplastic (CVISC) model introduced by Itasca [62], Paraskevopoulou and Diederichs [7, 23] presented LDP simulations for viscoelastic rock masses. However, in the CVISC model, the plastic slider is not coupled with viscous dashpot plastic yielding, which means that the model behaves similarly to a viscoelastic body if the stress states are below the yielding threshold [23]. However, in many engineering cases, it is essential to consider the coupling between the plastic behaviour and the creep behaviour of the rock mass.

In summary, research on this topic has been mostly concerned with elastic, plastic, viscoelastic, or viscoplastic problems. To overcome these limitations, in this paper, we present a new coupled ViscoElastic-ViscoPlastic Strain-Softening (VEVP-SS) model, which considers the following:

1. Time-dependent creep deformation.

2. Mohr-Coulomb and Hoek-Brown strain-softening models.

3. Progressive damage coupled with creep behaviour to simulate failure induced by creep and the subsequent progressive damage. This is the most significant part of the proposed model.

4. The existence of the ‘limited stress level’, which will be explained in section 2. Our approach intends to be a general numerical approach for obtaining the longitudinal deformation profile (LDP) of tunnels excavated in time-dependent strain-softening rock masses.

The coupled ViscoElastic-ViscoPlastic Strain-Softening (VEVP-SS) model is first introduced and implemented into the finite element software CODE_BRIGHT [63]. Numerical tests are carried out to calibrate the numerical implementation and to verify the coupled behaviour of viscous dashpot and strain-softening models. Then, the CODE_BRIGHT results are compared with analytical solutions and FLAC [62, 64] results to verify the viscoelastic and strain-softening behaviour in the VEVP-SS model, respectively. Finally, a comprehensive parameter analysis is provided to illustrate the sensitivity of the model to the excavation rate and rock mass behaviour model selection. It should be noted that the VEVP-SS model is currently under development, and further improvements are in progress. For example, a primary creep stage may be introduced in the VEVP-SS model in the near future.

2. Theoretical background

2.1. Rock mass behaviour

In many practical engineering problems, the actual behaviour of rock masses is governed by plastic and viscous effects [65]. Many creep tests on soft rocks show that the time-dependent deformation generally accounts for more than 30% of the total deformation, and in some cases, even up to 70% [17, 30, 66, 67]. Time dependency (also known as creep) results in deferred deformations and displacements, which must be taken into account to design underground projects more accurately and avoid safety issues in the working area [23, 41]. Moreover, the post-peak stress-strain behaviour of the rock mass may play a non-negligible role when a deep underground excavation is made [36]. Hoek and Brown [56] provided particularly relevant post-peak strength guidelines. These guidelines are based on the geotechnical quality of the rock mass described by the geotechnical strength index (GSI):

1. For high-quality rock masses (GSI > 70), the rock mass behaves in a purely brittle manner.

2. For average-quality rock masses (25 < GSI < 70), the rock mass presents strain-softening (SS) behaviour, *i.e.* after achieving a maximum stress, the rock mass can still withstand some load.

3. For very weak rock masses (GSI < 25), perfectly plastic behaviour is assumed [35], as shown in Figure 2a.

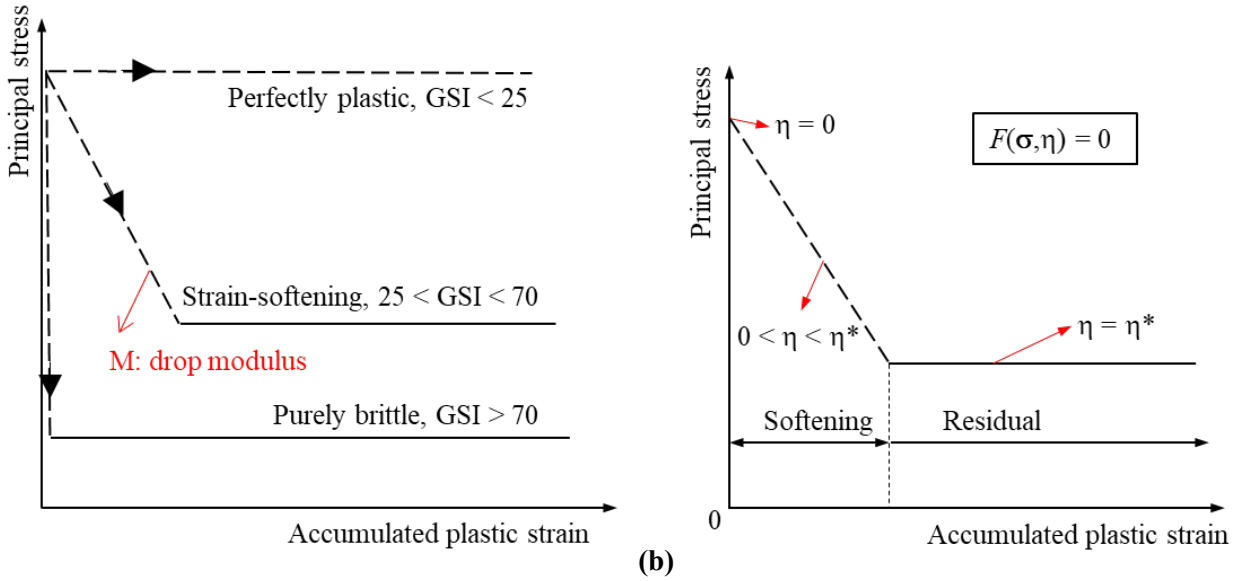

Figure 2. **(a)** Different post-failure behaviours of rock masses with different geological strength indexes (GSI); and **(b)** conceptual behaviour for a strain-softening model. Based on [35, 56].

Strain-softening behaviour can incorporate purely brittle behaviour (strain-softening with an infinite drop modulus, M, as shown in Figure 2a) and perfectly plastic behaviour (strain-softening with a drop modulus, M, equal to zero, as shown in Figure 2a). M represents the drop modulus of the strain-softening model, as shown in Figure 2a. Thus, perfectly plastic and purely brittle behaviours are just two particular cases of strain-softening behaviour.

In this paper, strain-softening models are adopted to simulate the post-failure behaviour of rock masses [26]. The yield surfaces $F(\boldsymbol{\sigma},\eta)$ for strain-softening models depend not only on the stress tensor $\boldsymbol{\sigma}$ but also on

the plastic or softening parameter η [24, 35], as shown in Figure 2b. Strain-softening behaviour is characterized by a gradual transition from the peak failure surface to the residual failure surface, which is governed by the plastic or softening parameter η. In a strain-softening model, a softening regime occurs whenever $0 < \eta < \eta^*$, and the residual regime takes place when $\eta \geq \eta^*$ [24, 35]. η^* is the value of the softening parameter at which the softening phase ends and the residual phase begins.

Figures 3a and 3b present the typical creep curves of a rock mass under a constant applied load based on experimental data [68] and a conceptual model, respectively. As shown in Figure 3b, the typical creep curves can be characterized by three stages:

1. Elastic stage: the elastic strain appears instantaneously upon loading, and the associated strains are fully reversible and transient [42].

2. Viscoelastic stage: the displacements are induced with time under a constant stress. In some research, the viscoelastic stage can also be divided into the primary creep stage (the strain rate decreases with time) and secondary creep stage (a constant strain rate with time). Note that although the load reversal would cause the specimen to return to the initial dimensions in the primary creep stage, the associated strain is irreversible in the secondary creep stage [42]. In this article, only secondary creep is considered, which is reasonable for some cases, such as rock salt [69, 70], rock masses under squeezing conditions [42], tunnels excavated in weak or altered rock masses [15] and very deep excavations [42].

3. Viscoelastic-viscoplastic stage (accelerated or tertiary creep stage): the strain rate starts to accelerate once the material starts to yield (damage). Viscoplastic strain occurs only when the stresses achieve a critical state, which can be defined by a yield surface $F = 0$. Hence, only elastic/viscoelastic deformations occur when $F < 0$, and viscoelastic-viscoplastic strains occur when $F \geq 0$ [7].

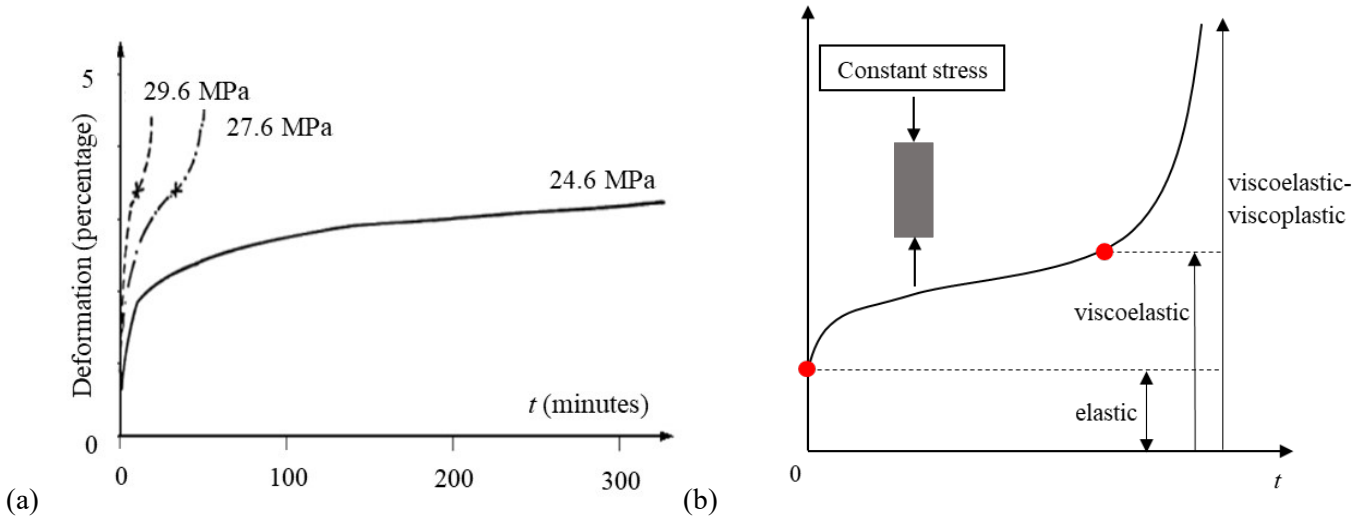

Figure 3. **(a)** Typical creep curve based on experimental data [68] and **(b)** the conceptual model of creep curves.

Figure 4a presents the typical stress-strain curves of creep tests [7]: after some incremental stress $\Delta\sigma$ is applied (points A, C or E), the applied load is kept constant for a long period of time. Note that there exists a 'limited stress level': for stress values below the 'limited stress level', no failure occurs, even with sufficient time (see line 'A-B' in Figure 4a). However, for stress states above the 'limited stress level', the stress state will result in failure. This failure will occur at different values of accumulated strain. In fact, the higher the stress is, the lower the value of the accumulated strain that leads to failure (see lines 'C-D' and 'E-F' in Figure 4a) and the faster this failure occurs [5-7].

In the present paper, a coupled ViscoElastic-ViscoPlastic Strain-Softening (VEVP-SS) model combined with strain-softening failure criteria (Mohr-Coulomb and Hoek-Brown) is proposed. As shown in Figure 5, these tentative approaches are needed if, as recommended by Starfield and Cundall [71], we follow heuristic approaches to study, analyse and understand rock mechanics problems.

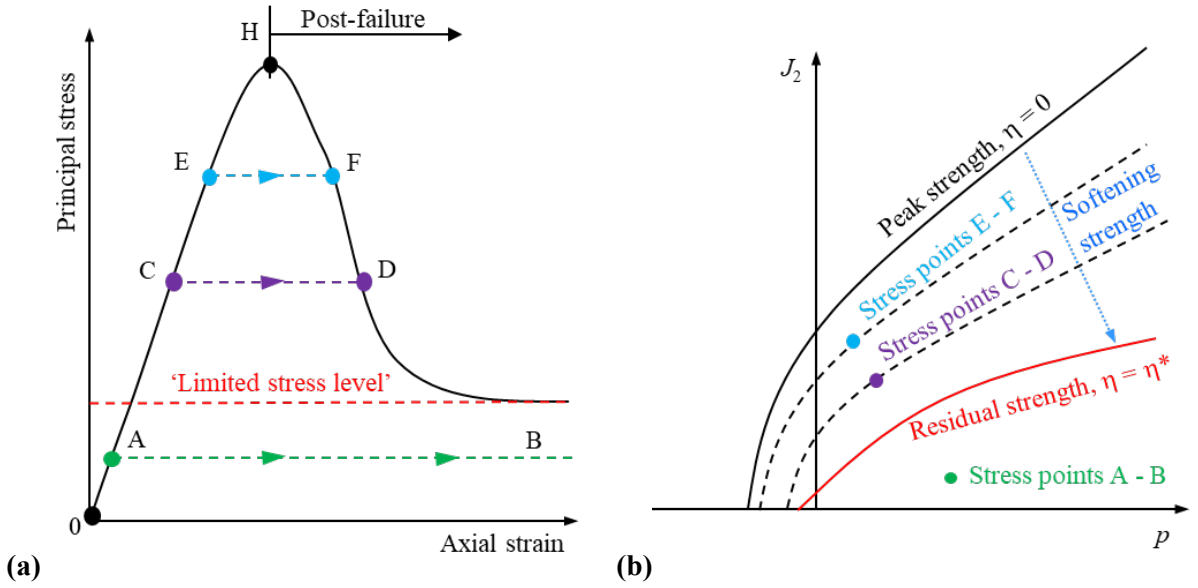

Figure 4. **(a)** Schematic representation of the long-term stress-strain response when subjected to constant stress conditions, and **(b)** yield surface evolution for a strain-softening rock mass.

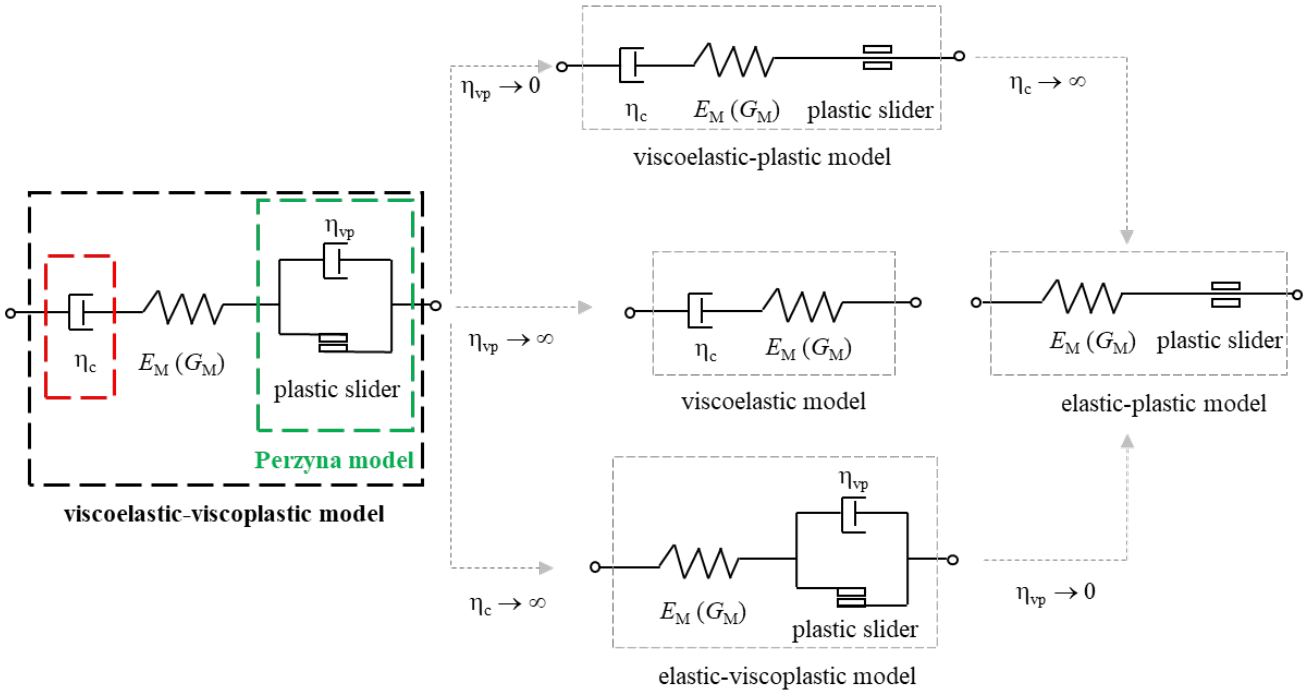

Figure 5. Comparison among five mechanical models for rocks.

2.2. A coupled ViscoElastic-ViscoPlastic Strain-Softening (VEVP-SS) model

In rock mechanics, Hookean elastic springs, Newtonian viscous dashpots, and plastic sliders are used to model a variety of rock mass behaviours [33]. The coupled ViscoElastic-ViscoPlastic Strain-Softening (VEVP-SS) model consists of an elastic spring and a viscous dashpot in series with the Perzyna viscoplastic model.

Figure 5 shows five common typical mechanical models of a rock mass, where E_M (G_M) is the elastic (shear) modulus of the rock mass; η_c and η_{vp} represent the viscosities of the viscous dashpot and the Perzyna model, respectively; and the parameters for the plastic slider depend on the failure criteria chosen. As shown in Figure 5, four different models can be considered as particular cases of the VEVP-SS model: the viscoelastic model, by assigning a sufficiently large value to η_{vp}; the elastic-viscoplastic model, by assigning a sufficiently large value to η_c; the viscoelastic-plastic model, by assigning a sufficiently small value to η_{vp}; and the elastic-plastic model, by assigning a sufficiently large value to η_c and a sufficiently small value to η_{vp}. Note that the concepts of 'sufficiently large' and 'sufficiently small' denote infinite and zero, respectively, for practical numerical reasons that do not significantly affect the results.

The total strain rate tensor $\frac{d\boldsymbol{\varepsilon}}{dt}$ of the proposed VEVP-SS model can be decomposed into components describing the rock elasticity ($\frac{d\boldsymbol{\varepsilon}_e}{dt}$) and inelasticity ($\frac{d\boldsymbol{\varepsilon}_i}{dt}$), as shown in Eq. (1).

$$\frac{d\boldsymbol{\varepsilon}}{dt} = \frac{d\boldsymbol{\varepsilon}_e}{dt} + \frac{d\boldsymbol{\varepsilon}_i}{dt} \tag{1}$$

where $\boldsymbol{\varepsilon}_e$ and $\boldsymbol{\varepsilon}_i$ represent the elastic and inelastic strain tensors, respectively. The elastic strain rate can be expressed in Eq. (2).

$$\frac{d\boldsymbol{\varepsilon}_{\mathrm{e}}}{dt}=\frac{\mathbf{m}}{3K_{\mathrm{M}}}\frac{dp}{dt}+\frac{1}{2G_{\mathrm{M}}}\left(\frac{d\boldsymbol{\sigma}}{dt}-\frac{dp}{dt}\mathbf{m}\right) \tag{2}$$

where $K_{\mathrm{M}}=\frac{E_{\mathrm{M}}}{3(1-2\nu)}$ and $G_{\mathrm{M}}=\frac{E_{\mathrm{M}}}{2(1+\nu)}$ represent the volumetric stiffness and deviatoric stiffness, respectively; ν represents Poisson's ratio; and $\boldsymbol{\sigma} = p\mathbf{m} + \mathbf{s}$, in which $\boldsymbol{\sigma}$ (p) represents the stress (mean stress) matrix and $\mathbf{m} = [1\ 1\ 1\ 0\ 0\ 0]^{\mathrm{T}}$. The inelastic strain is the sum of the viscous (creep) strain $\boldsymbol{\varepsilon}_{\mathrm{c}}$ and the viscoplastic strain $\boldsymbol{\varepsilon}_{\mathrm{vp}}$, *i.e.,* $\boldsymbol{\varepsilon}_{\mathrm{i}}=\boldsymbol{\varepsilon}_{\mathrm{c}}+\boldsymbol{\varepsilon}_{\mathrm{vp}}$. As shown in Figure 5, the viscous dashpot is adopted to simulate the creep behaviour of rock masses. The Perzyna model, consisting of a viscous dashpot in parallel with a plastic slider, can simulate the viscoplastic behaviour of rock masses. Thus, the inelastic strain rate can be expressed by Eq. (3), where $\eta_{\mathrm{c}}^{\mathrm{v}}$ ($\eta_{\mathrm{c}}^{\mathrm{d}}$) represents the volumetric (deviatoric) viscosity of the viscous dashpot, η_{vp} represents the viscosity of the viscoplastic model and F and G represent the overstress function and the viscoplastic potential, respectively, of the viscoplastic model.

$$\frac{d\boldsymbol{\varepsilon}_{\mathrm{i}}}{dt}=\frac{d\boldsymbol{\varepsilon}_{\mathrm{c}}}{dt}+\frac{d\boldsymbol{\varepsilon}_{\mathrm{vp}}}{dt}=\frac{\mathbf{m}}{3\eta_{\mathrm{c}}^{\mathrm{v}}}p+\frac{1}{2\eta_{\mathrm{c}}^{\mathrm{d}}}(\boldsymbol{\sigma}-p\mathbf{m})+\frac{1}{\eta_{\mathrm{vp}}}\langle\Phi(\mathrm{F})\rangle\frac{\partial G}{\partial\boldsymbol{\sigma}} \tag{3}$$

$$\langle\Phi(F)\rangle=\begin{cases}0, & \text{for } F\le 0\\ \Phi(F), & \text{for } F>0\end{cases} \tag{4}$$

The form of $\Phi(F)$ can be defined by experimental data [65]. For simplicity, $\Phi(F) = F^{\mathrm{m}}$ ($\mathrm{m} \ge 1$) is adopted in this paper. Overstress theory [22, 65] has been adopted for the Perzyna viscoplastic model and is different from purely plastic theory. Overstress theory allows the stress point to exceed the yield surface. As shown in Figure 6, the yield surface sets the limits of two different regimes in the stress space:

1. If the stress point is below the yield surface, the rock mass exhibits non-viscoplastic behaviour, *i.e.,* elastic or viscoelastic behaviour in the proposed model.

2. If the stress point is between the yield surface and the viscoplastic limit, the rock mass will exhibit viscoplastic properties. The viscoplastic limit is related to the viscosity of the Perzyna viscoplastic model, *i.e.,* η_{vp} in Eq. (3). As the viscosity η_{vp} is closer to zero, the viscoplastic limit will be closer to the yield surface *F*. It must be noted again that one can always ensure a viscoplastic solution as close as necessary to the 'true' purely plastic solution by sufficiently decreasing the viscosity η_{vp} of the viscoplastic formulation [72].

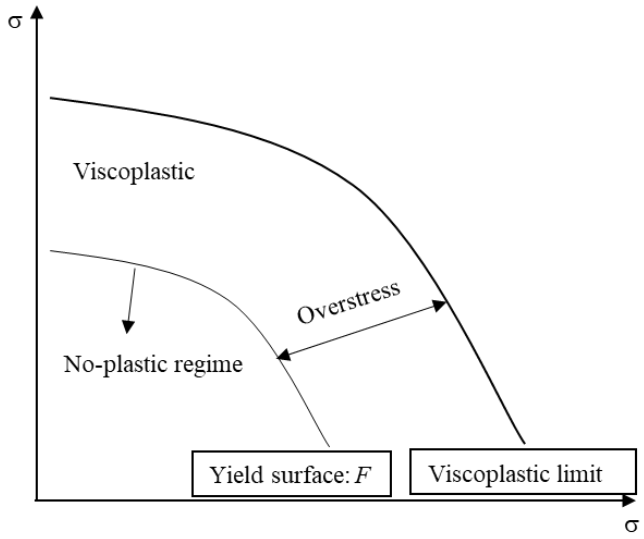

Figure 6. Overstress theory of the viscoplastic model.

In rock masses, deviatoric stress states cause deviatoric strain rates that may produce significant long-term deformations, while the volumetric strain is less significant [30]. Thus, only the deviatoric part of the viscosity (η_c^d) has been considered, and the volumetric viscosity (η_c^v) has not been considered. In the VEVP-SS model, the overstress function is assumed to be equal to the viscoplastic yield function (failure criterion). Thus, the total strain rate can be expressed by Eq. (5).

$$\frac{d\boldsymbol{\varepsilon}}{dt}=\frac{d\boldsymbol{\varepsilon}_{\mathrm{e}}}{dt}+\frac{d\boldsymbol{\varepsilon}_{\mathrm{c}}}{dt}+\frac{d\boldsymbol{\varepsilon}_{\mathrm{vp}}}{dt}=\frac{\mathbf{m}}{3K_{\mathrm{M}}}\frac{dp}{dt}+\frac{1}{2G_{\mathrm{M}}}\left(\frac{d\boldsymbol{\sigma}}{dt}-\frac{dp}{dt}\mathbf{m}\right)+\frac{1}{2\eta_{\mathrm{c}}^{\mathrm{d}}}(\boldsymbol{\sigma}-p\mathbf{m})+\frac{1}{\eta_{\mathrm{vp}}}\left\langle F^{\mathrm{m}}\right\rangle\frac{\partial G}{\partial\boldsymbol{\sigma}} \tag{5}$$

It should be noted that in our proposed VEVP-SS model, only the secondary creep stage is considered in the viscoelastic model; hence, the associated creep strain $\boldsymbol{\varepsilon}_{\mathrm{c}}$ is irreversible [39, 42]. Then, it is reasonable to assume that failure may be reached by accumulated creep deformation (*e.g.*, from point E to point F in Figure 4). To make this failure depend on the stress history and the applied stress, the viscoplastic yield surface is assumed to evolve from a peak failure criterion to a residual one (which we refer to as softening). Furthermore, after failure, both creep strain $\boldsymbol{\varepsilon}_{\mathrm{c}}$ and viscoplastic strain $\boldsymbol{\varepsilon}_{\mathrm{vp}}$ accumulate in our proposed model to account for the strain-softening behaviour (*e.g.*, from point F to the residual stage in Figure 4). This coupling constitutes the most important part and the most significant novelty of the VEVP-SS model. Hence, the proposed VEVP-SS model can be used to simulate the creep-induced failure shown in Figure 4 and the coupled behaviour between creep deformation and damage evolution.

In the VEVP-SS model, as shown in Figure 4b, the peak and residual yield surfaces define 3 different fields in the stress space:

1. The viscoelastic field below the residual yield surface, where the strain rates are $\frac{d\boldsymbol{\varepsilon}_{\mathrm{e}}}{dt}+\frac{d\boldsymbol{\varepsilon}_{\mathrm{c}}}{dt}$ (*e.g.,* stress point B in Figure 4b with a stress-strain behaviour represented by the line '0-A-B' in Figure 4a).

2. The field between the peak and residual yield surfaces, where the deformations are initially viscoelastic (*e.g.,* points C and E in Figure 4a) but will then become viscoelastic-viscoplastic when the yield surfaces eventually decreases to the stress point (*e.g.,* points D and F in Figure 4a).

3. The viscoelastic-viscoplastic field on/above the peak yield surface (*e.g.,* point H in Figure 4a), where the deformations can be divided into elastic, creep and viscoplastic parts, $\frac{d\boldsymbol{\varepsilon}_{\mathrm{e}}}{dt}+\frac{d\boldsymbol{\varepsilon}_{\mathrm{c}}}{dt}+\frac{d\boldsymbol{\varepsilon}_{\mathrm{vp}}}{dt}$.

In this paper, a linearly decreasing function of the plastic parameters k(η) is adopted to represent the strain-softening behaviour [24, 35], as shown in Eq. (6), where $\mathrm{k}_{\mathrm{peak}}$ and $\mathrm{k}_{\mathrm{res}}$ are the peak and residual values of k, respectively. If a Mohr-Coulomb failure surface is considered, k represents the cohesion c and friction angle φ, while k represents the m_{HB} and s_{HB} parameters when considering the Hoek-Brown failure surface.

$$\mathrm{k}(\eta)=\begin{cases}\mathrm{k}_{\mathrm{peak}}, & \text{for } \eta<0\\ \mathrm{k}_{\mathrm{peak}}+\left(\dfrac{\mathrm{k}_{\mathrm{res}}-\mathrm{k}_{\mathrm{peak}}}{\eta^{*}}\right)\eta, & \text{for } 0\le\eta<\eta^{*}\\ \mathrm{k}_{\mathrm{res}}, & \text{for } \eta\ge\eta^{*}\end{cases} \tag{6}$$

Note that when considering a Mohr-Coulomb failure criterion, the relationship between the friction angle φ and its tangent (tanφ) can be assumed to be approximately linear for the typical range of friction angle values for rock masses (< 30 deg). Nevertheless, we selected a linear decrease in the friction angle to represent softening, following the work of other researchers that used a linearly decreasing function for the friction angle [20, 24, 35, 36, 49, 73].

The softening parameter η is defined as shown in Eq. (7), where $\boldsymbol{\varepsilon}^{\mathrm{p}}$ ($\boldsymbol{\gamma}^{\mathrm{p}}$) represents the accumulated plastic strain and $\varepsilon_{\mathrm{m}}^{\mathrm{p}}=\frac{1}{3}\left(\varepsilon_{\mathrm{x}}^{\mathrm{p}}+\varepsilon_{\mathrm{y}}^{\mathrm{p}}+\varepsilon_{\mathrm{z}}^{\mathrm{p}}\right)$.

$$\eta=\sqrt{\frac{3}{2}\left[\left(\varepsilon_{\mathrm{x}}^{\mathrm{p}}-\varepsilon_{\mathrm{m}}^{\mathrm{p}}\right)^{2}+\left(\varepsilon_{\mathrm{y}}^{\mathrm{p}}-\varepsilon_{\mathrm{m}}^{\mathrm{p}}\right)^{2}+\left(\varepsilon_{\mathrm{z}}^{\mathrm{p}}-\varepsilon_{\mathrm{m}}^{\mathrm{p}}\right)^{2}+\left(\frac{1}{2}\gamma_{\mathrm{xy}}^{\mathrm{p}}\right)^{2}+\left(\frac{1}{2}\gamma_{\mathrm{yz}}^{\mathrm{p}}\right)^{2}+\left(\frac{1}{2}\gamma_{\mathrm{zx}}^{\mathrm{p}}\right)^{2}\right]} \tag{7}$$

The expression of the Mohr-Coulomb strain-softening failure criterion is shown in Eq. (8), where c(η) and φ(η) are the plastic strain-dependent cohesion and the friction angle, respectively. p, J_2 (J_3) and θ represent the mean stress, the second (third) invariable stress, and the Lode angle, respectively.

$$F_{\mathrm{MC}} = p\sin\varphi(\eta) + \sqrt{J_2}\left(\cos\theta - \frac{1}{\sqrt{3}}\cdot\sin\varphi(\eta)\cdot\sin\theta\right) - c(\eta)\cos\varphi(\eta) \tag{8}$$

The expression of the Hoek-Brown strain-softening failure criterion is shown in Eq. (9), where $m_{\mathrm{HB}}(\eta)$ and $s_{\mathrm{HB}}(\eta)$ are the plastic strain-dependent parameters of the Hoek-Brown failure criterion and σ_{ci} is the uniaxial compressive strength of the intact rock.

$$F_{\mathrm{HB}} = \left[\frac{4}{\sigma_{\mathrm{ci}}}\cos^2\theta\sqrt{J_2} + \frac{2}{\sqrt{3}}m_{\mathrm{HB}}(\eta)\cos\left(\theta + \frac{\pi}{6}\right)\right]\sqrt{J_2} - m_{\mathrm{HB}}(\eta)\left[-p + \frac{s_{\mathrm{HB}}(\eta)\sigma_{\mathrm{ci}}}{m_{\mathrm{HB}}(\eta)}\right] \tag{9}$$

The Mohr-Coulomb form of the potential has been considered in both the Mohr-Coulomb and Hoek-Brown strain-softening models [35, 36], as expressed in Eq. (10), where α is a parameter for the potential ($0 \le \alpha \le 1$) and ψ is the dilatancy angle.

$$G = \alpha p\sin\psi + \sqrt{J_2}\left(\cos\theta - \frac{1}{\sqrt{3}}\sin\psi\sin\theta\right) \tag{10}$$

The total number of constitutive parameters of the ViscoElastic-ViscoPlastic Strain-Softening (VEVP-SS) model is 12, as shown in Table 1: 2 classical elastic parameters, 1 viscous (creep) parameter, and 9 viscoplastic parameters. The only clear disadvantage of the VEVP-SS model is the inability to simulate the primary creep stage; thus, the use of the VEVP-SS model should be limited to cases in which large deformation occurs due to secondary and accelerated creep and the primary creep-induced deformation is negligible, such as tunnelling excavation in weak, altered or hard rock masses or very deep tunnelling excavation [15, 42].

Table 1. Constitutive parameters of the VEVP-SS model.

Elastic	E_M (G_M)	Elastic (shear) modulus
	ν	Poisson's ratio
Viscous	η_c	Viscosity of the viscous dashpot
Viscoplastic	η_{vp}	Viscosity of the Perzyna model
	m	Stress power
	η^*	The critical softening parameter
	ψ	Dilatancy angle
	α	Associativity parameter
	c_{peak}, c_{res}, φ_{peak}, φ_{res}	Parameters for the Mohr-Coulomb strain-softening model
	m_{peak}, m_{res}, s_{peak}, s_{res}	Parameters for the Hoek-Brown strain-softening model

3. Numerical implementation

The proposed ViscoElastic-ViscoPlastic Strain-Softening (VEVP-SS) model was implemented into the finite element method software CODE_BRIGHT. CODE_BRIGHT [63] was developed at the Department of Civil and Environmental Engineering of the Technical University of Catalonia (UPC) and works in combination with the pre-/post-processor GID, developed by the International Centre for Numerical Methods in Engineering (CIMNE). If another code is adopted, the same constitutive model presented in this paper can be utilized. The implementation of the proposed VEVP-SS model should consider the following aspects: (1) the existence of corners in the yield (and potential) surfaces at which the gradients are not uniquely defined, and thus requiring smoothing methods; (2) the development of strain-softening and localization.

3.1. Smoothing method of the failure criteria and the potential

Due to the gradient discontinuities in both the Mohr-Coulomb and Hoek-Brown failure criteria, we found that the developed numerical implementations suffered from non-convergence issues as well as excessive CPU time consumption. Therefore, to overcome these problems, smoothing methods have been adopted to round both yield surfaces and the potential function. Expressions of both the Mohr-Coulomb failure surface and the potential function were based on a smoothing method described in the scientific literature [74, 75]. On the other hand, it should be noted that the smoothed Hoek-Brown failure surface was derived in this paper (Appendix A).

The smoothed Mohr-Coulomb strain-softening yield surface [75] shown in Eq. (11) was adopted in the current research, where $a = m_{mc}c(\eta)\cot\varphi(\eta)$, and a is typically defined as 0.25.

$$F_{\mathrm{MC}} = \sqrt{J_2 K_{\mathrm{MC}}^2(\theta) + a^2 \sin^2\varphi(\eta)} + p\sin\varphi(\eta) - c(\eta)\cos\varphi(\eta) \tag{11}$$

As the value of the hyperbolic parameter m_{MC} approaches zero, the yield surface approaches a hyperbolic shape [75]. In addition, an alternative form of $K_{MC}(\theta)$ in the vicinity of the singularities was defined to round the failure surface function F [75], as shown in Eq. (12), where θ_T is a specified transition angle, typically defined as 25 deg.

$$K_{\mathrm{MC}}(\theta,\eta) = \begin{cases} A_{\mathrm{MC}} + B_{\mathrm{MC}}\sin 3\theta, & \text{for } |\theta| > \theta_{\mathrm{T}} \\ \cos\theta - \dfrac{1}{\sqrt{3}}\sin\varphi(\eta)\sin\theta, & \text{for } |\theta| \le \theta_{\mathrm{T}} \end{cases} \tag{12}$$

where:

$$A_{\mathrm{MC}} = \frac{1}{3}\cos\theta_{\mathrm{T}}\left[3 + \tan\theta_{\mathrm{T}}\tan 3\theta_{\mathrm{T}} + \frac{1}{\sqrt{3}}\langle\theta\rangle\left(\tan 3\theta_{\mathrm{T}} - 3\tan\theta_{\mathrm{T}}\right)\sin\varphi(\eta)\right]$$

$$B_{\mathrm{MC}} = -\frac{1}{3\cos 3\theta_{\mathrm{T}}}\left[\langle\theta\rangle \sin\theta_{\mathrm{T}} + \frac{1}{\sqrt{3}}\sin\varphi(\eta)\cos\theta_{\mathrm{T}}\right]$$

$$\langle\theta\rangle = \begin{cases} +1, & \theta \geq 0 \\ -1, & \theta < 0 \end{cases}$$

Since the second derivative of the plastic potential should also be continuous, the C2 method [74] was used to smooth the potential function. Following the method of Abbo et al. [74], the smoothed potential was adopted, which can be expressed as shown in Eq. (13). The alternative form of $K_{\mathrm{G}}(\theta)$ in the vicinity of the singularities can be expressed as shown in Eq. (14), where θ_{T} is a specified transition angle, typically defined as 25 deg.

$$G = \alpha p \sin\psi + J_2 K_{\mathrm{G}}^2(\theta) \tag{13}$$

$$K_{\mathrm{G}}(\theta) = \begin{cases} D_{\mathrm{G}} + E_{\mathrm{G}}\sin 3\theta + F_{\mathrm{G}}\sin^2 3\theta, & \text{for } |\theta| > \theta_{\mathrm{T}} \\ \cos\theta - \frac{1}{\sqrt{3}}\sin\psi\sin\theta, & \text{for } |\theta| \leq \theta_{\mathrm{T}} \end{cases} \tag{14}$$

where

$$F_{\mathrm{G}} = \frac{-\cos 3\theta_{\mathrm{T}}\left(\cos\theta_{\mathrm{T}} - \frac{1}{\sqrt{3}}\sin\psi\langle\theta\rangle\right) - 3\langle\theta\rangle\sin 3\theta_{\mathrm{T}}\left(\langle\theta\rangle\sin\theta_{\mathrm{T}} + \frac{1}{\sqrt{3}}\sin\psi\cos\theta_{\mathrm{T}}\right)}{18\cos^3 3\theta_{\mathrm{T}}}$$

$$E_{\mathrm{G}} = \frac{\langle\theta\rangle\sin 6\theta_{\mathrm{T}}\left(\cos\theta_{\mathrm{T}} - \frac{1}{\sqrt{3}}\sin\psi\langle\theta\rangle\sin\theta_{\mathrm{T}}\right) - 6\cos 6\theta_{\mathrm{T}}\left(\langle\theta\rangle\sin\theta_{\mathrm{T}} + \frac{1}{\sqrt{3}}\sin\psi\cos\theta_{\mathrm{T}}\right)}{18\cos^3 3\theta_{\mathrm{T}}}$$

$$D_{\mathrm{G}} = -\frac{1}{\sqrt{3}}\sin\psi\langle\theta\rangle\sin\theta_{\mathrm{T}} - E\langle\theta\rangle\sin 3\theta_{\mathrm{T}} - F\sin^2 3\theta_{\mathrm{T}} + \cos\theta_{\mathrm{T}}$$

These equations were adapted from Abbo et al. [74] and Abbo and Sloan [75]. The reader is referred to the original source for a detailed description of the smoothed approximation (C1 and C2) to the Mohr-Coulomb failure surface.

However, the smoothed approximation to the Hoek-Brown yield surface was derived in the current research and is presented in Eq. (15), and the alternative form of $K_{HB}(\theta, \eta)$ in the vicinity of the singularities can be expressed as Eq. (16), where θ_T is a specified transition angle, typically defined as 25 deg.

$$F_{HB} = K_{HB}(\theta,\eta)\sqrt{J_2} - m_{HB}(\eta)\left[-p + \frac{s_{HB}(\eta)\sigma_{ci}}{m_{HB}(\eta)}\right] \tag{15}$$

$$K_{HB}(\theta,\eta) = \begin{cases} A_{HB} + B_{HB}\sin 3\theta, & \text{for } \theta \geq |\theta_T| \\ \dfrac{4}{\sigma_{ci}}\cos^2\theta\sqrt{J_2} + \dfrac{2}{\sqrt{3}}m_{HB}(\eta)\cos\left(\theta + \dfrac{\pi}{6}\right), & \text{for } \theta \leq |\theta_T| \end{cases} \tag{16}$$

where

$$A_{HB} = m_{HB}(\eta)\left[\left(\cos\theta_T - \frac{\langle\theta\rangle\sin\theta_T}{\sqrt{3}}\right) + \left(\frac{\cos\theta_T}{3\sqrt{3}} + \frac{1}{3}\langle\theta\rangle\sin\theta_T\right)\langle\theta\rangle\tan 3\theta_T\right]$$
$$+ \sqrt{J_2}\left[\frac{4\cos^2\theta_T}{\sigma_{ci}} + \frac{8\sin\theta_T\cos\theta_T\tan 3\theta_T}{3\sigma_{ci}}\right]$$
$$B_{HB} = \sqrt{J_2}\left(-\frac{8\langle\theta\rangle\sin\theta_T\cos\theta_T}{3\sigma_{ci}\cos 3\theta_T}\right) - \frac{m_{HB}(\eta)}{3\cos 3\theta_T}\left(\langle\theta\rangle\sin\theta_T + \frac{\cos\theta_T}{\sqrt{3}}\right)$$

Note that the expressions of A_{HB} and B_{HB} were obtained by matching the zero and first derivatives for the rounded surface to those for the Hoek-Brown surface at θ_T and $-\theta_T$. Appendix A presents the derivation of the smoothed Hoek-Brown failure criterion.

3.2. Strength parameter update and strain localization

In the proposed VEVP-SS model, the strength parameters are the cohesion and friction angle if the Mohr-Coulomb failure surface is chosen or m_{HB} and s_{HB} if the Hoek-Brown failure surface is chosen. A specific implementation has been developed to compute the accumulated plastic (unrecoverable) strain $\boldsymbol{\varepsilon}^{\mathbf{p}}$, *i.e.,* the

sum of the viscous strain $\boldsymbol{\varepsilon_c}$ and viscoplastic strain $\boldsymbol{\varepsilon_{vp}}$, in this model. For the elements in the numerical model, the accumulated unrecoverable strain is updated, and then the softening parameter η is updated based on Eq. (7). Finally, the strength parameters are updated following the function of Eq. (6), and the failure surface is updated.

As shown in Figure 4b, the peak residual strength surfaces divide the stress space into 3 fields:

1. For the elements where the stress state is below the residual strength, the accumulated unrecoverable strain ($\boldsymbol{\varepsilon}^p$) is equal to the viscous strain $\boldsymbol{\varepsilon_c}$, *i.e.,* $\boldsymbol{\varepsilon}^p = \boldsymbol{\varepsilon_c}$. Therefore, the response will be only viscoelastic in this case, even if the strength parameters are updated.

2. For the elements where the stress state is between the peak and residual strength surfaces, the accumulated strain is equal to the viscous (creep) strain at the beginning of the simulation, and the strength parameters are updated with the increase in the accumulated creep strain (as well as the softening parameter η). Thus, the failure surface shrinks with increasing η, and the stress state could then meet the failure surface if η is sufficiently large. After that, the accumulated unrecoverable strain is assumed to be a combination of viscous and viscoplastic strains ($\boldsymbol{\varepsilon}^p = \boldsymbol{\varepsilon_c} + \boldsymbol{\varepsilon_{vp}}$).

3. For the elements where the stress state is on/above the peak strength, the accumulated unrecoverable strain is assumed to be a combination of viscous and viscoplastic strains, *i.e.,* $\boldsymbol{\varepsilon}^p = \boldsymbol{\varepsilon_c} + \boldsymbol{\varepsilon_{vp}}$, and thus, their response would be viscoelastic-viscoplastic. The softening parameters can be updated based on Eq. (7), when the unrecoverable strain is obtained.

Nonetheless, softening behaviour may introduce numerical difficulties. In some cases, instability occurs because softening concentrates at isolated elements, while other elements in their vicinity experience stress relaxation. However, the viscoplastic approach that is adopted for our strain-softening model is capable of homogenizing the spatial distribution of softening strain, which benefits the control of the size of the

localized zone and thus allows avoidance of the dependency on the employed mesh [22, 72]. In addition, from an engineering point of view, strain localization effects are not relevant when considered on an appropriately large spatial scale [26], as would be the case of the tunnel excavation model in this article. In section 4.2, an analysis of the effect of mesh quality on the resulting tunnel deformation is carried out.

4. Numerical verification

To verify the numerical implementation, an example of a creep test was first carried out to verify the coupled behaviour between the creep model and the strain-softening model. After that, a number of 2D axisymmetric numerical models were employed to assess the performance of the viscoplastic model in tunnel excavation, including a mesh-independence analysis. Finally, the viscoelastic part and the strain-softening part of the proposed VEVP-SS model were verified separately by comparison with analytical solutions [34, 43] and FLAC numerical results [36], respectively.

4.1 Verification of the coupled behaviour

As we explained in section 2, the most important novelty of the VEVP-SS model is the coupled behaviour between the creep model and the strain-softening model. Hence, a triaxial creep numerical test was carried out to analyse the coupled behaviour implemented in CODE_BRIGHT. Note that the analyses made do not represent any particular experiment, and the conditions and parameters adopted in the simulation were simply chosen to evaluate the key aspects of the coupled behaviour.

The model used here is 2D axisymmetric with dimensions of 0.014 m × 0.1 m. The normal displacements along the bottom and left boundaries were restrained, as shown in Figure 7a. In addition, constant stresses were applied along the right and top boundaries, with values of P_x = 0.2 MPa and P_y = 1.0 MPa,

respectively. A mesh with 600 quadratic triangle elements was considered for the analysis, as shown in Figure 7b. The calculation was stopped at 0.3 hours. In this sub-section, the Mohr-Coulomb strain-softening model was adopted for this example, and the parameters input into the numerical simulations are listed in Table 2.

In Figure 8, the results of the viscoelastic (VE) model and the ViscoElastic-ViscoPlastic Strain-Softening (VEVP-SS) model are compared. At the start of the simulation, stress point A (Figure 7a) is inside the viscoelastic domain, as shown in Figure 8a, so only viscoelastic strain occurs. Hence, initially, a steady creep takes place under constant stress, with the viscoelastic strain in the x and y directions increasing similarly for both the VE and VEVP-SS models, with the chosen point A maintains a constant stress under the constant stress condition imposed.

However, as the accumulated plastic (unrecoverable) strain increases, the yield surface decreases due to softening induced by creep (*i.e.* the softening parameter η develops due to the accumulated viscoelastic strain $\boldsymbol{\varepsilon}_c$). Consequently, when the yield surface reaches the point of our analysis, the strain rate accelerates due to both the creep and viscoplastic contributions. Figure 8b presents the softening process in terms of the cohesion and friction angle. Based on the numerical analysis, it can be concluded that creep behaviour is coupled with plastic behaviour in the proposed VEVP-SS model.

For further calibration, a series of biaxial creep tests were carried out to analyse the relationship between the principal strain and the applied stress. The numerical geometry and mesh quality are the same as in the former example, as shown in Figure 7. In the biaxial creep tests, $P_x = 0.0$ MPa, and six different stresses were considered, $P_y = 19.6$ MPa, 24.5 MPa, 29.4 MPa, 34.3 MPa, 36.0 MPa and 37.0 MPa. The calculation was stopped at 20 days. The input parameters are presented in Table 3, and these parameters were estimated with the intent of matching experimental data from the scientific literature [42, 76]. Figure 9 shows the time-dependent strains of the point (0, 0.1). In Figure 9, it shows that different stresses result in different

strains, and a higher applied stress will result in larger deformation, which is consistent with the conclusion of laboratory tests [42, 76]. If the input parameters are properly chosen, the proposed VEVP-SS model results can match experimental results.

Table 2. Mechanical properties of the rock mass in the numerical triaxial creep tests.

Input parameters for the ViscoElastic-ViscoPlastic Strain-Softening (VEVP-SS) model						
Peak cohesion, c_{peak} (MPa)	Residual cohesion, c_{res} (MPa)	Peak friction angle, φ_{peak} (deg)	Residual friction angle, φ_{res} (deg)	The critical softening parameter, η^*	Stress power, m	η_{vp} (MPa^{m}s)
0.2	0.1	30	15	0.02	3	10
Associativity parameter, α	Dilatancy angle, ψ (deg)	Elastic modulus, E_M (MPa)	Poisson's ratio, v	η_c^d (MPa s)	a in F_{MC}	θ_T (deg) for F and G
0	0	10^3	0.3	10^4	0.25	25

Table 3. Mechanical properties of the rock mass in the numerical biaxial creep tests.

Input parameters for the ViscoElastic-ViscoPlastic Strain-Softening (VEVP-SS) model						
Peak cohesion, c_{peak} (MPa)	Residual cohesion, c_{res} (MPa)	Peak friction angle, φ_{peak} (deg)	Residual friction angle, φ_{res} (deg)	Softening parameters, η^*	Stress power, m	Dilatancy angle, ψ (deg)
7.88	3.5	37.6	20	0.5	5	2.5
Elastic modulus, E_M (MPa)	Poisson's ratio, v	Associativity parameter, α	η_c^d (MPa s)	η_{vp} (MPa^{m}s)	a	θ_T (deg) for F and G
7056.4	0.3	1.0	1.5×10^{10}	5×10^9	0.25	25

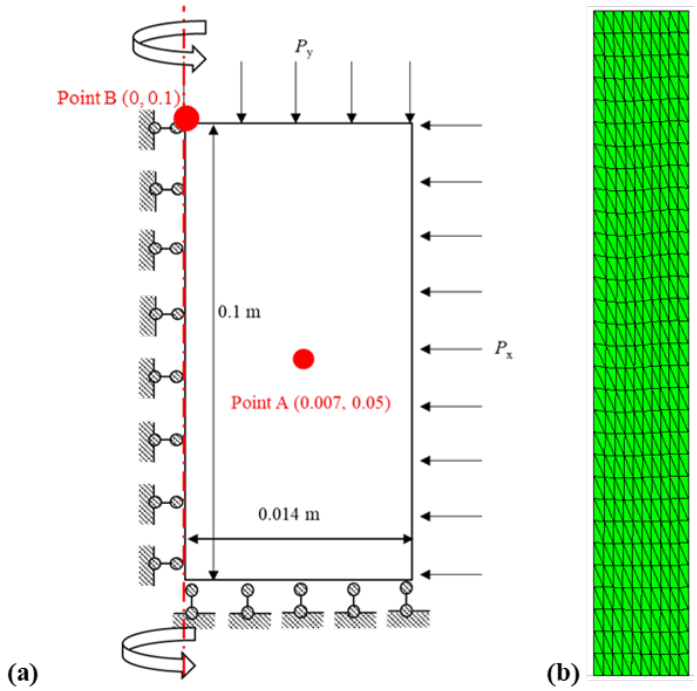

Figure 7. Creep numerical test: **(a)** basic features and boundary conditions (not real scale), and **(b)** mesh quality (real scale).

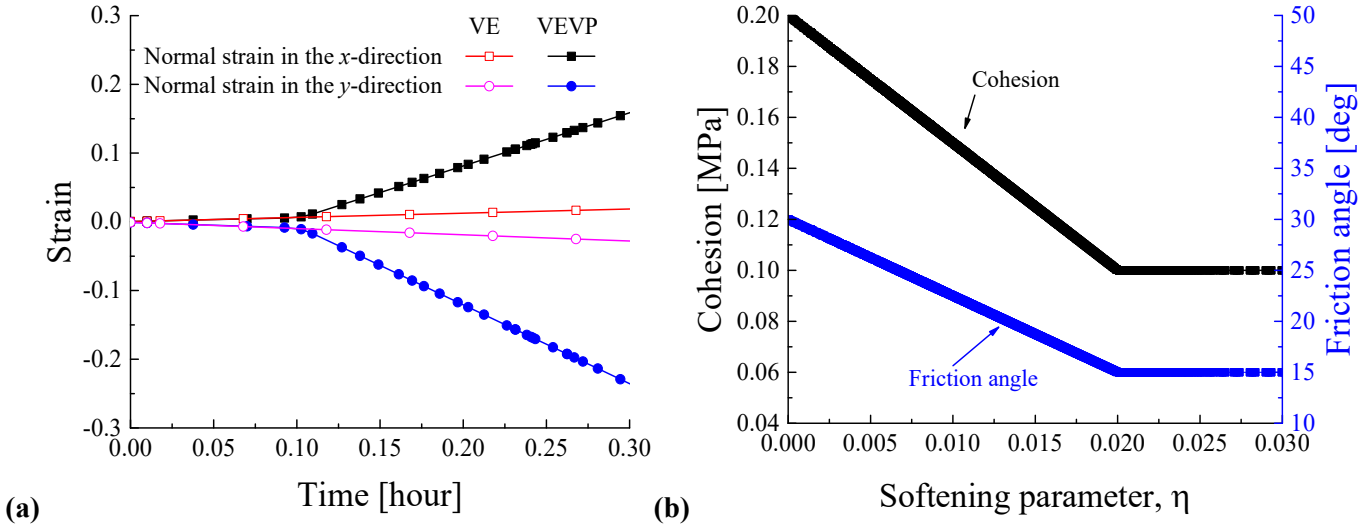

Figure 8. **(a)** Normal strain in the *x* and *y* directions for the viscoelastic (VE) and ViscoElastic-ViscoPlastic Strain-Softening (VEVP-SS) models at point A in Figure 7a. **(b)** Strength parameters (cohesion and friction angle in the Mohr-Coulomb strain-softening model) versus the softening parameter (η) at point A in Figure 7a.

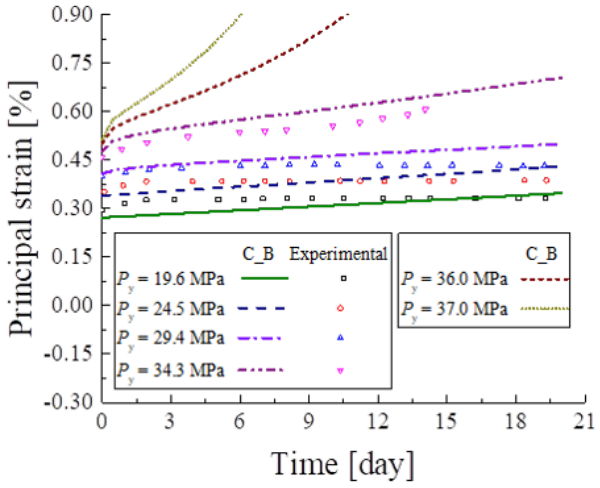

Figure 9. Numerical examples of creep tests for six different applied stresses. C_B represents CODE_BRIGHT numerical results.

4.2 Mesh independency

As previously mentioned in section 3, numerical analysis involving softening problems may exhibit a marked dependency on the finite element mesh employed. In this section, a number of 2D axisymmetric models were developed to assess the performance of the viscoplastic approach in the simulation of softening problems. In these models, a deeply buried tunnel with a diameter of 5 m is excavated in an elastic-viscoplastic ($\eta_c \rightarrow \infty$) and low-quality rock mass (GSI_{peak} = 40, GSI_{res} = 27), exhibiting a strong strain-softening behaviour. The rock specific weight is 25 kN/m^3 and the rest of the input parameters concerning this low-quality rock mass are shown in Table 4. Moreover, two different values of viscosity were adopted ($\eta_{vp} = 10^2$ MPa^{5}s and $\eta_{vp} = 10^4$ MPa^{5}s) to assess the influence of viscoplastic viscosity on mesh independency.

Furthermore, the tunnel is presented as a rectangle with a length of 55 m (Figure 10) so that 22 excavation steps of 2.5 m in length can be performed. The tunnel is excavated at a depth of 1500 m, implying a field

stress of 37.5 MPa. Hence, the normal displacements are fixed along the axisymmetric axis ($x = 0$) and on the bottom of the model ($y = 0$), and a pressure of 37.5 MPa is applied to the other boundaries of the model.

As shown in Figure 11, four meshes with different qualities were adopted to analyse the effect of mesh quality on the resulting displacements. The meshes are composed of the following number of quadratic triangular elements (*i.e.,* triangles with 6 nodes): (a) 988, (b) 2016, (c) 3719, and (d) 6342.

Finally, Figure 12 presents the longitudinal (axial) deformation versus the distance to the tunnel face for the aforementioned four meshes (mesh_01, mesh_02, mesh_03 and mesh_04) and for two different values of the viscoplastic viscosity η_{vp} ($\eta_{vp} = 10^2$ MPa^{5}s and $\eta_{vp} = 10^4$ MPa^{5}s). The good agreement shown among the results obtained with different mesh qualities verifies the mesh-independency of the proposed strain-softening model in tunnel design applications.

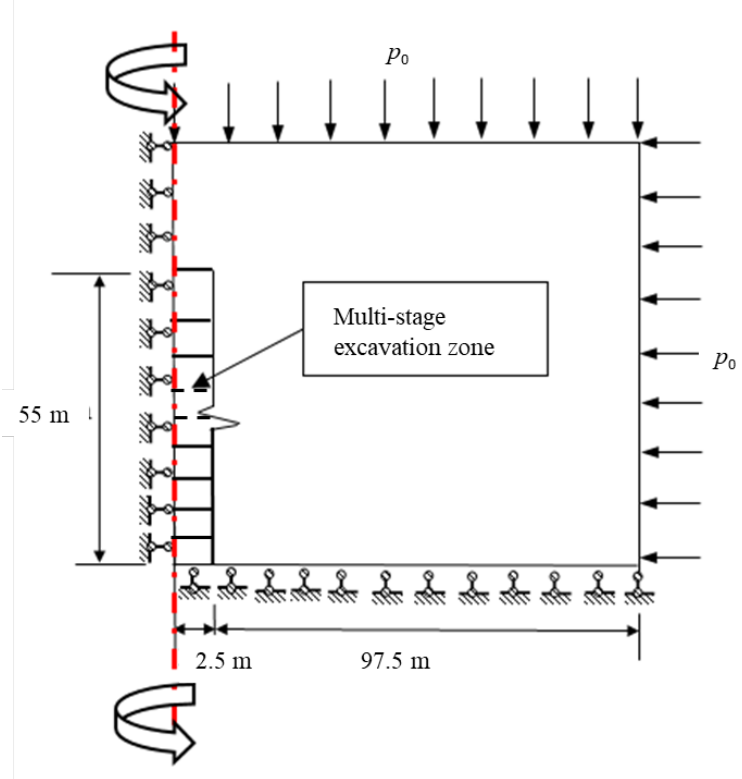

Figure 10. Basic features and boundary conditions for the 2D axisymmetric excavation model.

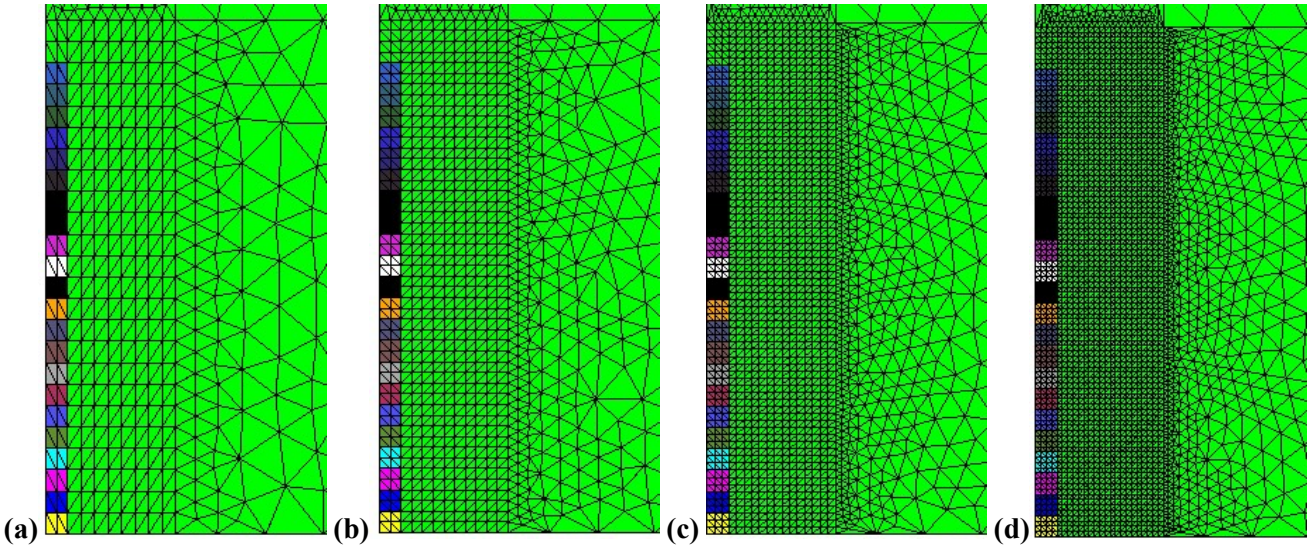

Figure 11. Four different mesh qualities used in the numerical analysis. The meshes are composed of the following number of quadratic triangular elements: (a) mesh_01: 988 elements, (b) mesh_02: 2016 elements, (c) mesh_03: 3719 elements, and (d) mesh_04: 6342 elements.

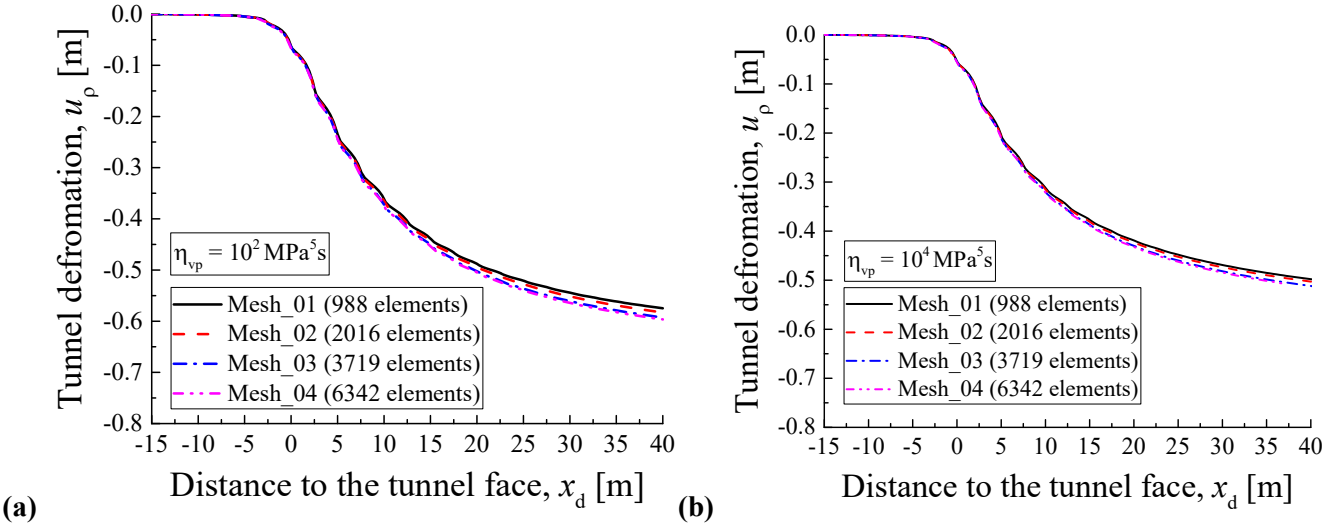

Figure 12. Longitudinal (axial) deformation u_ρ versus the distance to the tunnel face x_d for (a) $\eta_{vp} = 10^2$ MPa^{5}s and (b) $\eta_{vp} = 10^4$ MPa^{5}s. Four different mesh qualities (mesh_01, mesh_02, mesh_03 and mesh_04) are adopted for each case.

Table 4. Input parameters of the ViscoElastic-ViscoPlastic Strain-Softening (VEVP-SS) model.

Input parameters of the ViscoElastic-ViscoPlastic Strain-Softening (VEVP-SS) model							
Different quality of rock masses					High	Medium	Low
GSI			Peak		60	50	40
			Residual		35	30	27
Elastic parameters		Elastic modulus		E_M (MPa)	15400	8660	4870
		Poisson's Ratio		ν	0.25	0.25	0.25
Viscoelastic parameters		Deviatoric viscosity		η_c^d (MPa s)	∞	∞	∞
Viscoplastic parameters		Stress power		m	5	5	5
		Viscosity of the Perzyna model		η_{vp} ($MPa^m s$)	10^2 (*)	10^2 (*)	10^2 (*)
		θ_T for F and G		θ_T (deg)	25	25	25
	Post-failure behaviour	Hoek-Brown	Peak values	m_{HB}	1.68	1.17	0.821
				s_{HB}	0.0110	0.0039	0.0013
			Residual values	m_{HB}	0.687	0.575	0.516
				s_{HB}	0.0007	0.0004	0.0003
		Mohr-Coulomb	Peak values	c (MPa)	2.67	2.24	1.88
				φ (deg)	25.7	23.1	20.6
			Residual values	c (MPa)	1.71	1.54	1.43
				φ (deg)	19.4	18.2	17.5
			Smoothing parameter	a	0.25	0.25	0.25
		Critical softening parameters		η^*	0.0062	0.0288	0.119
	Plastic potential	Associativity parameter		α	1.0	1.0	1.0
		Dilatancy angle		ψ (deg)	4.49	2.89	1.55

(*) Sufficiently small value of η_{vp} to make the solution comparable to the purely plastic case

4.3. Verification of the viscoelastic model

The VEVP-SS model can be simplified to a viscoelastic model, as shown in Figure 5. To verify the viscoelastic model, an example of a circular tunnel excavated in a viscoelastic rock mass is carried out in CODE_BRIGHT. The numerical results are compared with the analytical solutions of Wang et al. [34, 43], who presented analytical solutions for circular tunnels with a time-dependent boundary [34, 43]. The expressions for tunnels excavated in Maxwell viscoelastic geomaterials under isotropic initial stresses are shown in Eq. (17), where G_{M} and $\eta_{\mathrm{c}}^{\mathrm{d}}$ are the deviatoric stiffness (shear modulus) and the deviatoric viscosity of the Maxwell viscoelastic model, respectively. R represents the time-dependent radius of the tunnel section; t represents time; p_0 represents the initial stress; u_ρ represents the incremental radial displacements that occurred during the excavation along the radial axis; and ρ represents the radial location in polar coordinates (ρ, θ), where $\rho = 0$ represents the location of the tunnel centre.

$$u_\rho(t) = -\frac{p_0}{2\rho}\int_0^t \left[\frac{1}{G_{\mathrm{M}}}\delta(t-\tau) + \frac{1}{\eta_{\mathrm{c}}^{\mathrm{d}}}\right] R^2(\tau)\, d\tau \tag{17}$$

The numerical model developed using CODE_BRIGHT is consistent with the hypothesis made in the analytical model, and both of them are calculated under plane-strain conditions with small deformation. Only a quarter of the tunnel structure is analysed in the numerical model (Figure 13) because of the double symmetry of the geometry and the boundary conditions on both the x and y axes. Moreover, the normal displacements along the bottom ($y = 0$) and the left ($x = 0$) boundaries are restrained. Figure 14 shows the mesh of the numerical model in the vicinity of the tunnel. A mesh of 764 quadratic triangular elements was adopted, with finer elements near the excavation. The initial stresses in the model are $p_0 = 20$ MPa. For the rock mass, $G_{\mathrm{M}} = 2000$ MPa, and $\eta_{\mathrm{c}}^{\mathrm{d}} = 8.64 \times 10^8$ MPa s. The first section of the tunnel was instantaneously

excavated at time equal to zero, $t = 0$ day. The following sections of the tunnel were excavated step by step, and the radius of the tunnel cross-section can be expressed by Eq. (18).

$$R(t) = \begin{cases} 2\,\text{m}, & \text{for} \quad 0 \le t < 5 \ \text{days} \\ 4\,\text{m}, & \text{for} \quad 5 \ \text{days} \le t < 10 \ \text{days} \\ 6\,\text{m}, & \text{for} \quad 10 \ \text{days} \le t < 15 \ \text{days} \\ 8\,\text{m}, & \text{for} \quad t \ge 15 \ \text{days} \end{cases} \tag{18}$$

After the completion of all excavation steps, the calculation was stopped at $t = 30$ days.

A comparison of the time-dependent incremental radial displacements that occurred during the excavation along the radial axis (u_ρ) predicted by the analytical solutions and the numerical simulations is shown in Figure 15 for points A, B, and C (see Figure 13). A good agreement between the numerical and analytical results is observed, verifying the viscoelastic model in CODE_BRIGHT.

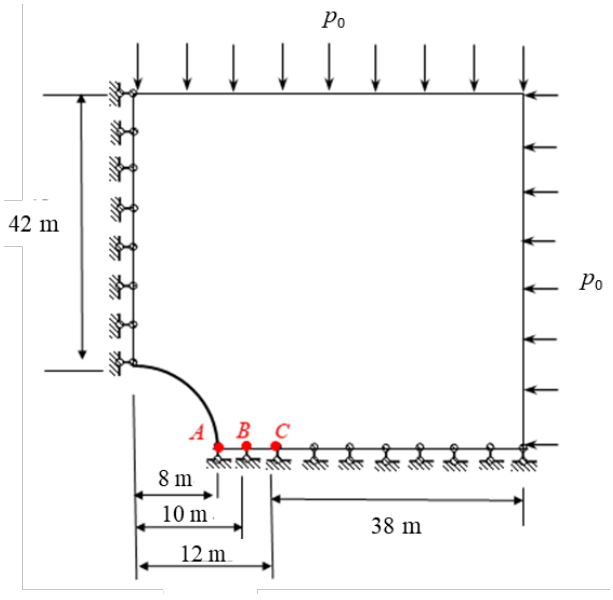

Figure 13. Basic features and boundary conditions for the plane-strain excavation model.

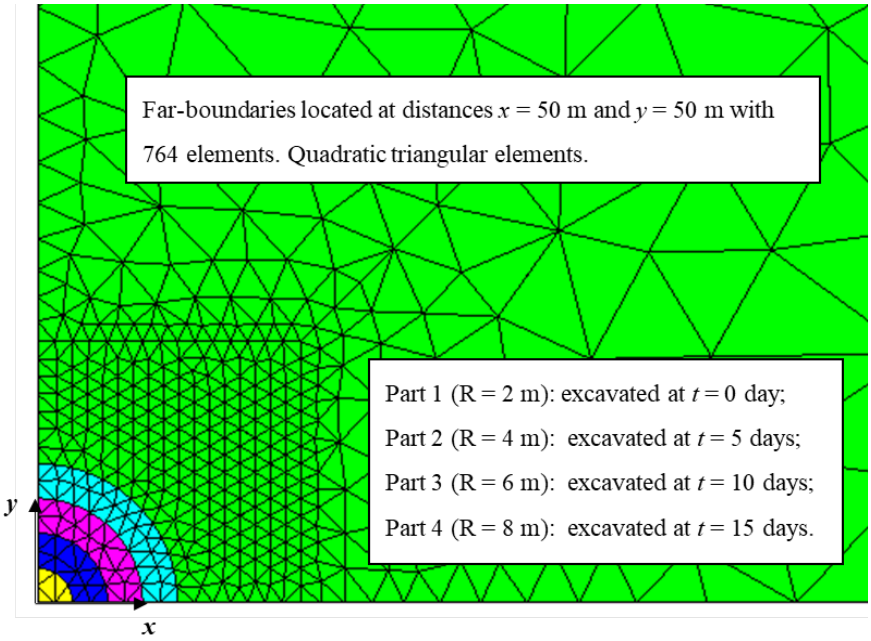

Figure 14. Mesh and geometry of the plane-strain excavation model.

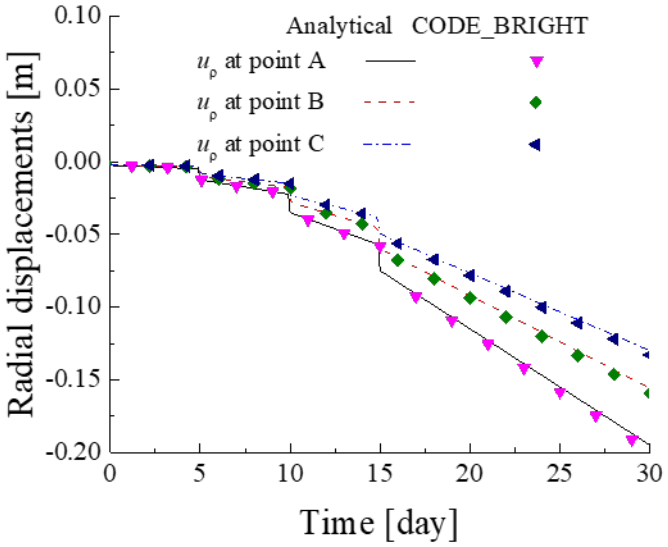

Figure 15. Comparison between analytical solutions [34, 43] and CODE_BRIGHT results for the incremental radial displacements u_ρ.

4.4. Verification of the strain-softening model

The VEVP-SS model can be simplified to the elastic-plastic strain-softening model by applying a sufficiently small η_{vp} and a sufficiently large η_c, as shown in Figure 5. To verify the theory and implementation of the strain-softening model, the results of the longitudinal deformation profile (LDP) obtained from CODE_BRIGHT are compared with the FLAC results from Alejano et al. [36]. The numerical model developed using CODE_BRIGHT is made to be consistent with the one described by Alejano et al. [36], and both of the models are solved using the elastic-plastic strain-softening model.

In the simulation, the geometry, boundary conditions, initial field stress and excavation process are the same as those described in section 4.2. The rock masses were weak intact rock, with $m_i = 7$ and $\sigma_{ci} = 35$ MPa. Three rock masses with different geotechnical qualities (high, medium and low) were adopted in the comparison, and Table 4 shows the input parameters for these rock masses [36]. Considering the post-failure behaviour, simulations are performed using both perfectly plastic (PP) and strain-softening (SS) models. Moreover, both the Mohr-Coulomb and Hoek-Brown failure criteria are used. Mesh_02 (in Figure 11) is adopted in the following numerical analysis.

The FLAC2D and FLAC3D results from Alejano et al. [36] were used for the comparison with the CODE_BRIGHT results. Neumann boundary conditions were adopted in the FLAC2D numerical models, and the discretised area was 70 m × 100 m [36]. Dirichlet boundary conditions were adopted in the FLAC3D numerical models, and the discretised area was 60 m × 60 m × 60 m [36]. A more detailed description of the numerical models was provided by Alejano et al. [36]. In the comparison, the radial displacements u_ρ were normalized by the maximum radial displacements u_ρ^{max}, and the distance to the tunnel face x_d were normalized by the radius of the tunnel R.

Figures 16 and 17 show good agreement of the longitudinal deformation profile (LDP) obeying the Mohr-Coulomb perfectly plastic (MC-PP), Mohr-Coulomb strain-softening (MC-SS), Hoek-Brown perfectly plastic (HB-PP), and Hoek-Brown strain-softening (HB-SS) models between CODE_BRIGHT, FLAC2D and FLAC3D, verifying the implementation of the strain-softening model. The slight differences in Figure 17 between the CODE_BRIGHT, FLAC2D and FLAC3D results when using the HB failure criterion may be caused by the different smoothing methods of the Hoek-Brown failure criterion (as shown in section 3) and the use of different types of boundary conditions (Dirichlet versus Neumann).

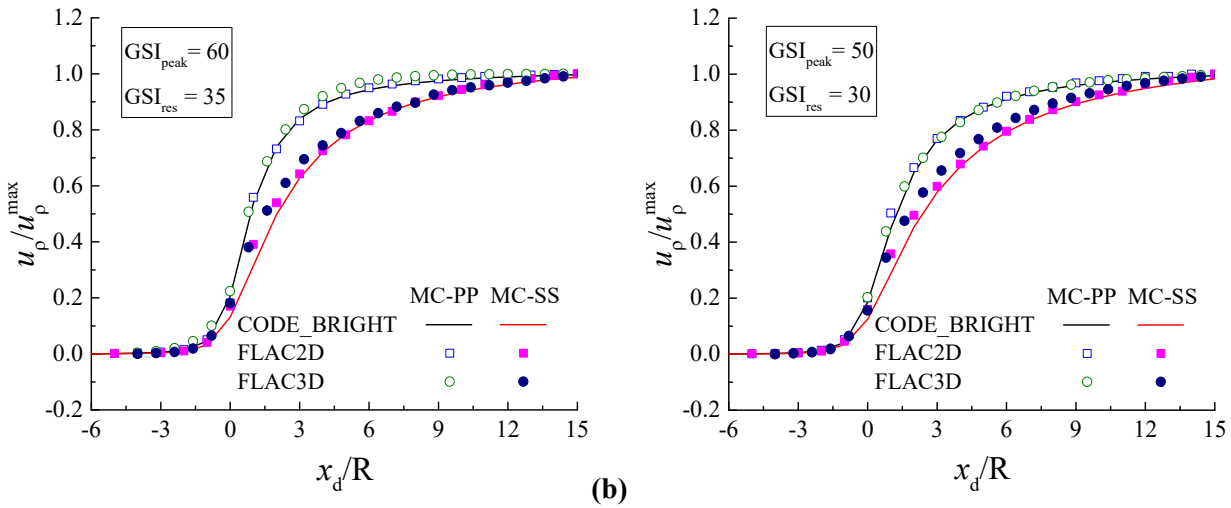

(a) **(b)**

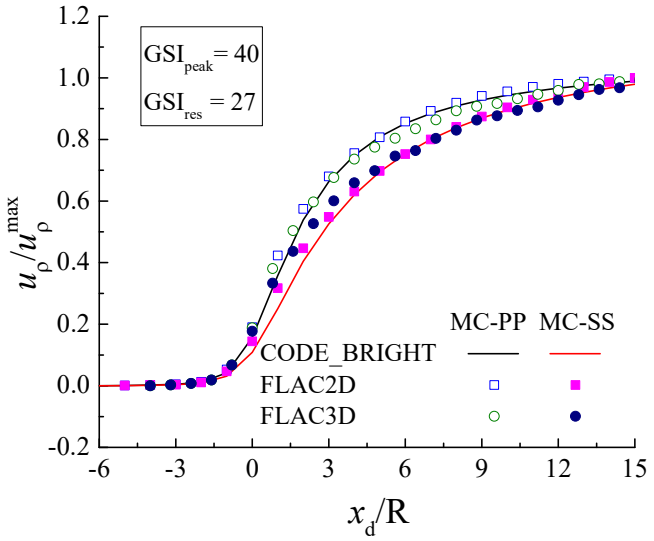

(c)

Figure 16. Comparison between FLAC results [36] and CODE_BRIGHT results for the normalized longitudinal deformation profile for three different rock mass qualities, (a) high-quality rock mass (GSI_{peak} = 60, GSI_{res} = 35), (b) medium-quality rock mass (GSI_{peak} = 50, GSI_{res} = 30), and (c) low-quality rock mass (GSI_{peak} = 40, GSI_{res} = 27), considering the Mohr-Coulomb perfectly plastic (MC-PP) and the Mohr-Coulomb strain-softening (MC-SS) behaviour models.

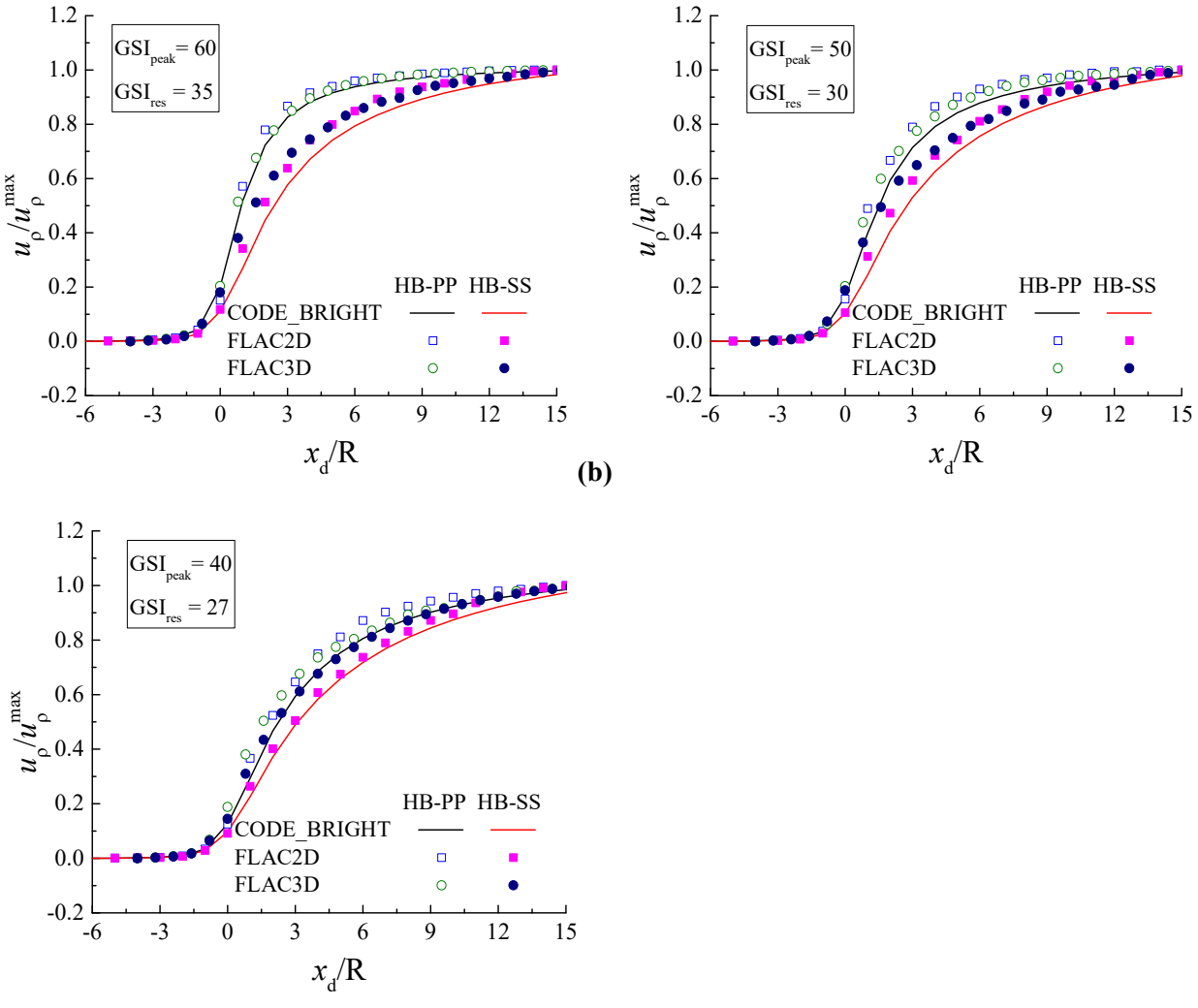

Figure 17. Comparison between FLAC results [36] and CODE_BRIGHT results for the normalized longitudinal deformation profile for three different rock mass qualities: (a) high-quality rock mass (GSI_{peak} = 60, GSI_{res} = 35), (b) medium-quality rock mass (GSI_{peak} = 50, GSI_{res} = 30), and (c) low-quality rock mass (GSI_{peak} = 40, GSI_{res} = 27), considering the Hoek-Brown perfectly plastic (HB-PP) and the Hoek-Brown strain-softening (HB-SS) behaviour models.

5. The application of the VEVP-SS model in the design of tunnels

The creep failure behaviour of rock may be relevant for many engineering cases, such as for some tunnels that do not fail during the process of tunnel excavation and support construction but ultimately fail after long-term operation [3, 77]. This phenomenon may be caused by the coupling between the creep behaviour and the strain-softening behaviour of rock masses, which can now be simulated by the proposed ViscoElastic-ViscoPlastic Strain-Softening (VEVP-SS) model.

As shown in Figure 18, if the VEVP-SS model is adopted to simulate the rock mass behaviour, the rock mass can be divided into two different zones: (1) viscoelastic zone and (2) viscoelastic-viscoplastic zone. In this section, an example is carried out to analyse the tunnelling excavation problems of deeply buried tunnels. The influence on the resulting longitudinal deformation profiles (LDPs) of several modelling features, such as the rock mass geotechnical quality (GSI), the post-failure behaviour model chosen, the viscosity introduced in the model, or the tunnel excavation rate, will be illustrated. Moreover, the examples show the potential applicability of the proposed VEVP-SS model.

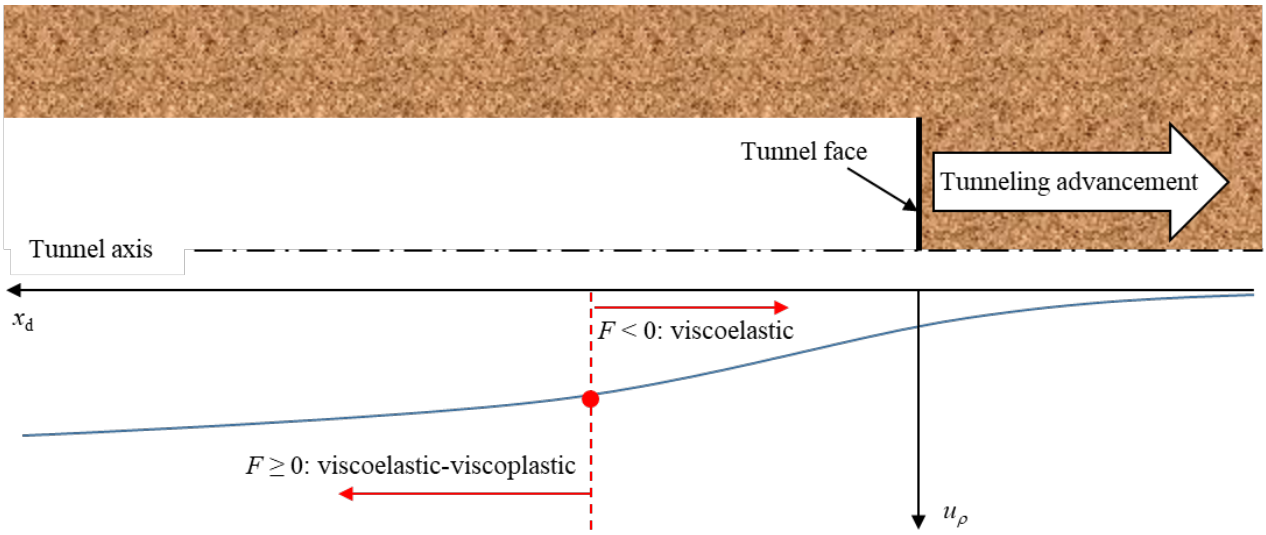

Figure 18. The longitudinal deformation profile (LDP) in a ViscoElastic-ViscoPlastic Strain-Softening (VEVP-SS) rock mass.

The excavated tunnel is 5 m in diameter and buried approximately 750 m deep. The initial in situ stress is assumed to be p_0 = 18.75 MPa. The numerical model geometry, boundary conditions, and excavation process (see Figure 10) are the same as those described in section 4.2. In the following numerical simulations, Mesh_02 with 2016 quadratic triangular elements is adopted, as shown in Figure 11b. Three different (high, medium and low quality) rock masses are considered, and the parameters of the rock masses, including (1) the elastic parameters, (2) the stress power, (3) the post-failure behaviour and (4) the potential, are shown in Table 4. To simplify the analysis, the radial displacements u_ρ are normalized by the corresponding maximum displacements of the elastic model $u^{\max}_{\rho,\text{elastic}}$, and the distance to the tunnel face x_d is normalized by the radius of the tunnel R. For the sake of comparison, two special cases that do not consider the time-dependent behaviour of the rock mass are presented in all of the following parametric analyses: (1) elastic behaviour and (2) elastic-plastic behaviour (EP).

5.1. Influence of the selection of rock mass behaviour models

The longitudinal deformation profiles (LDPs) of four different post-failure behaviour models are investigated: (1) the Mohr-Coulomb perfectly plastic (MC-PP), (2) the Mohr-Coulomb strain-softening (MC-SS), (3) the Hoek-Brown perfectly plastic (HB-PP), and (4) the Hoek-Brown strain-softening (HB-SS) models. In the example, the viscosities of the viscous and viscoplastic models are η_c^d = 10^{10} MPa s and η_{vp} = 10^4 MPa^{5}s, respectively. The excavation rate is 2.5 m/day.

Without considering the time-dependent behaviour of rock masses, *i.e.,* for the elastic and elastic-plastic (EP) models, Figure 19 shows the normalized longitudinal deformation profile along the normalized

distance to the tunnel face. For time-independent materials, the displacements first increases and then reaches a stable value when the distance to the tunnel face is large enough.

The LDP obeying the Hoek-Brown failure criterion is, from an engineering point of view, similar to the LDP obeying the Mohr-Coulomb failure criterion. Furthermore, it should be noted that the difference between the LDP calculated for perfectly plastic (PP) rock masses and for strain-softening (SS) rock masses increases as the GSI increases [36]. For high-quality rock masses, the LDP obtained is significantly different if we consider perfectly plastic or strain-softening behaviour, while this difference can be negligible for lower-quality rock masses, as expected, since PP behaviour accurately represents the behaviour of low-quality rock masses of GSI < 40 [35].

For viscoelastic-viscoplastic (VEVP) models, the displacements are caused not only by elastic and strain-softening processes but also by the creep behaviour of the rock mass; thus, the displacements keep increasing throughout the simulation, even at high x_d/R ratios. This can be a reasonable assumption for some cases: rock salt [67], rock masses under squeezing conditions [42], tunnels excavated in weak or altered rock masses [15] or very deep excavations [42].

Figures 20 and 21 present the longitudinal deformation profiles determined by using the elastic, elastic-plastic (EP) and viscoelastic-viscoplastic (VEVP) models, obeying the Mohr-Coulomb failure criterion and the Hoek-Brown failure criterion, respectively. The displacement results of the VEVP model are larger than the corresponding EP results, due to the additional contribution of the viscous (creep) behaviour.

At a great depth, stress redistributions due to tunnel excavation may lead to so-called squeezing conditions, both in low- and high-quality rock masses [39]. In this context, large deformations may develop due to secondary and tertiary creep, while the primary creep-induced deformation may be considered negligible [15]. Thus, the proposed ViscoElastic-ViscoPlastic Strain-Softening (VEVP-SS) model may be useful to reproduce the actual behaviour of rock masses under these conditions.

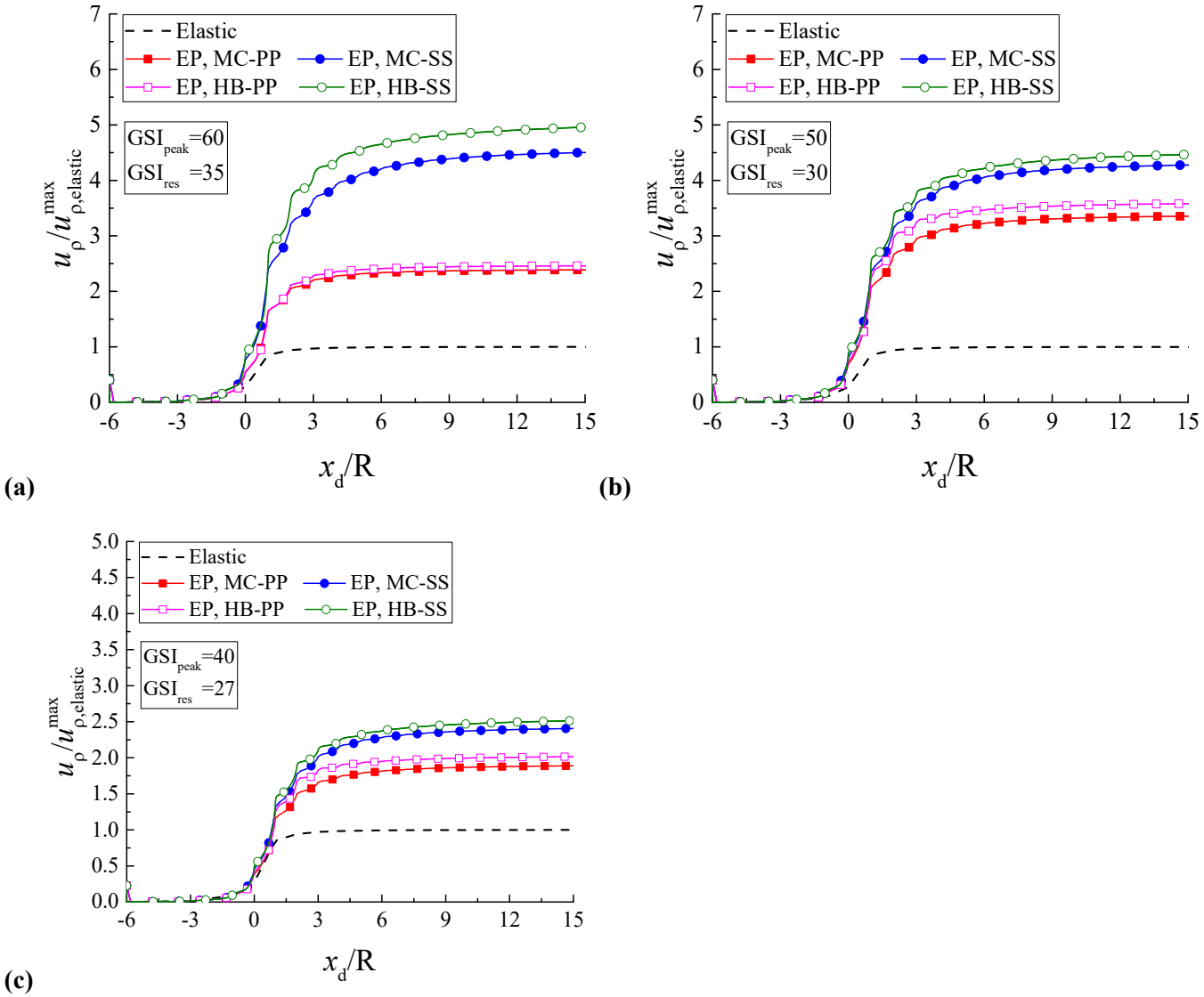

Figure 19. Normalized longitudinal deformation profiles along the normalized distance to the tunnel face by using elastic and elastic-plastic (EP) mechanical models; the Mohr-Coulomb (Hoek-Brown) perfectly plastic, *i.e.,* MC-PP (HB-PP), post-failure behaviour model; and the Mohr-Coulomb (Hoek-Brown) strain-softening, *i.e.,* MC-SS (HB-SS), post-failure behaviour model. Three different rock qualities are considered: (a) GSI_{peak}=60, GSI_{res}=35, (b) GSI_{peak}=50, GSI_{res}=30, and (c) GSI_{peak}=40, GSI_{res}=27.

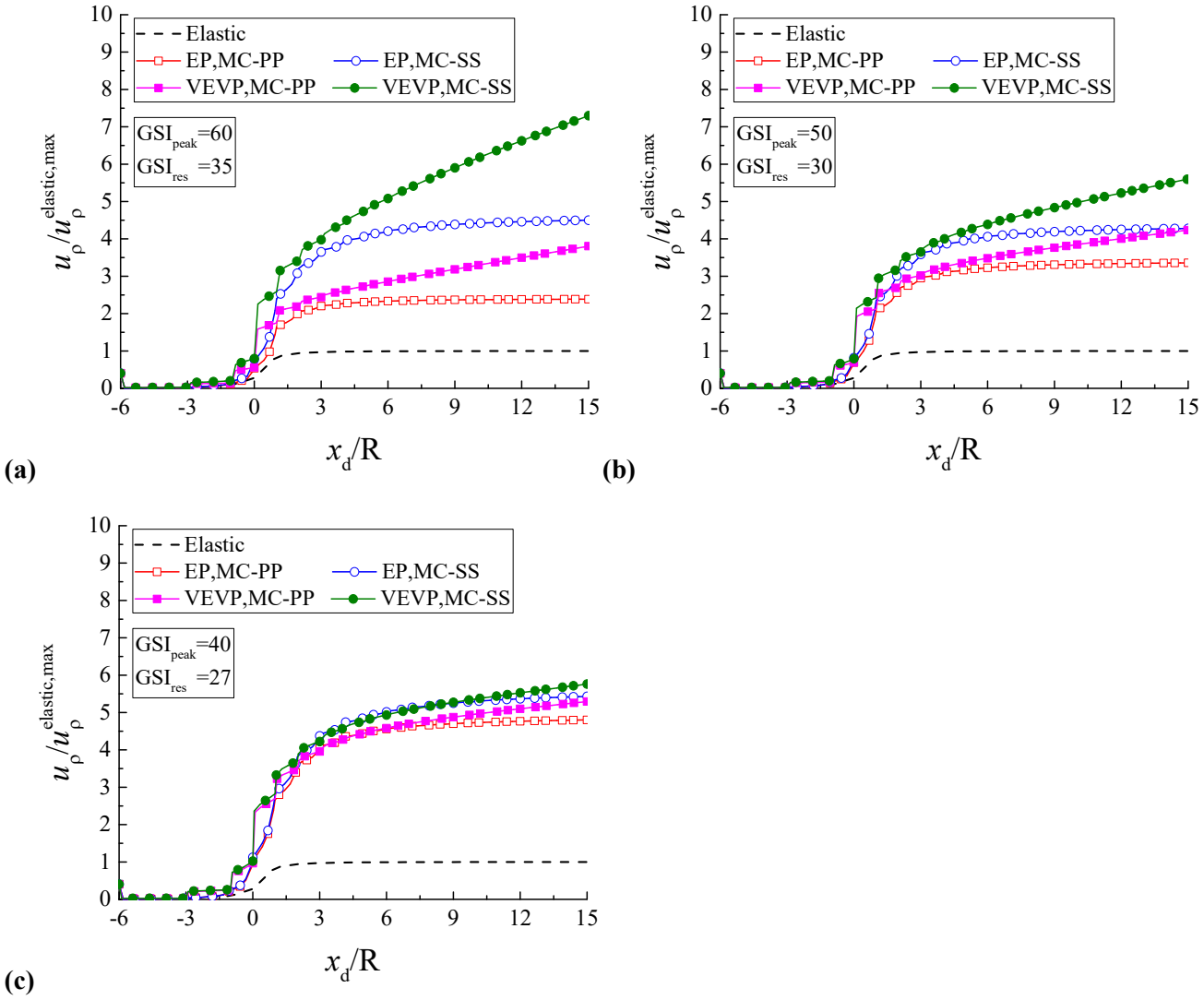

Figure 20. Normalized longitudinal deformation profiles along the normalized distance to the tunnel face by using the elastic, elastic-plastic (EP), and viscoelastic-viscoplastic (VEVP) mechanical models; the Mohr-Coulomb perfectly plastic (MC-PP) post-failure behaviour model; and the Mohr-Coulomb strain-softening (MC-SS) post-failure behaviour model. Three different rock qualities are considered: (a) GSI_{peak}=60, GSI_{res}=35, (b) GSI_{peak}=50, GSI_{res}=30, (c) GSI_{peak}=40, and GSI_{res}=27.

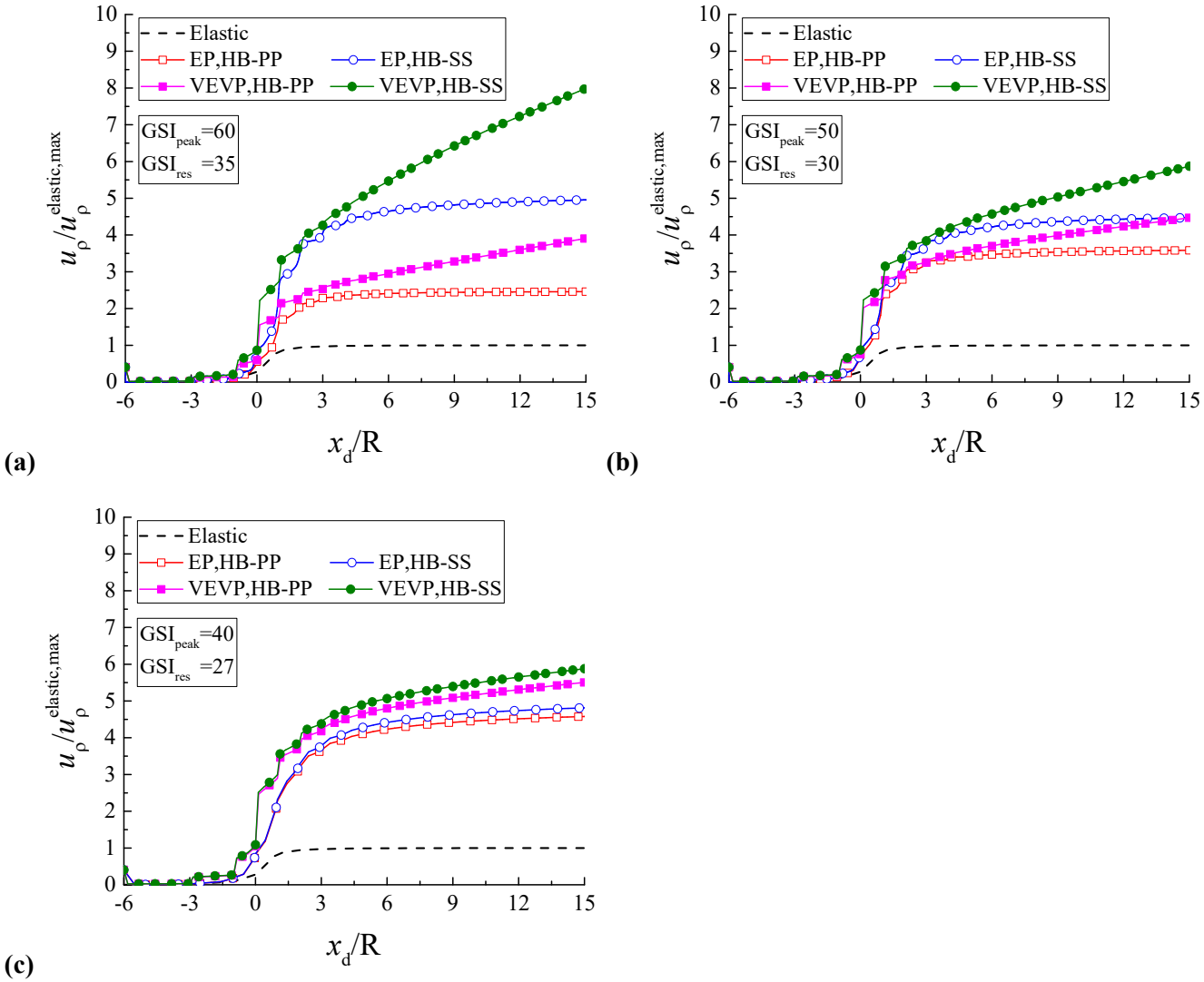

Figure 21. Normalized longitudinal deformation profiles along the normalized distance to the tunnel face by using the elastic, elastic-plastic (EP), and viscoelastic-viscoplastic (VEVP) mechanical models; the Hoek-Brown perfectly plastic (HB-PP) post-failure behaviour model; and the Hoek-Brown strain-softening (HB-SS) post-failure behaviour model. Three different rock qualities are considered: (a) GSI_{peak}=60, GSI_{res}=35, (b) GSI_{peak}=50, GSI_{res}=30, (c) GSI_{peak}=40, and GSI_{res}=27.

5.*2. Influence of the excavation rates*

To analyse the influence of the excavation rates on the resulting longitudinal deformation profiles (LDPs), three different excavation rates were considered: V = 0.83 m/day, V = 1.25 m/day and V = 2.5 m/day. The elastic, elastic-plastic (EP), and viscoelastic-viscoplastic (VEVP) models were considered. Both Mohr-Coulomb perfectly plastic (MC-PP) and Mohr-Coulomb strain-softening (MC-SS) post-failure behaviour models were adopted in this example. In the VEVP model, the viscosities of the viscous and viscoplastic models were $\eta_c^d = 10^{10}$ MPa s and $\eta_{vp} = 10^4$ MPa^{5}s, respectively.

Figures 22 and 23 show the LDP obeying the MC-PP and the MC-SS post-failure behaviour models, respectively. For the elastic and elastic-plastic rock masses, the LDP is identical for different excavation rates, *i.e.,* the elastic and elastic-plastic LDPs are only related to the distance to the tunnel face x_d. However, for the viscoelastic-viscoplastic rock masses, the shapes of the LDPs are very different for different excavation rates, and the displacements do not achieve a steady state in this case due to the contribution of the creep deformation. Lower excavation rates may lead to larger displacements because there is more time for creep deformation to develop. The difference between the longitudinal deformation profiles (LDPs) calculated for elastic-plastic rock masses and for viscoelastic-viscoplastic rock masses increases with the GSI.

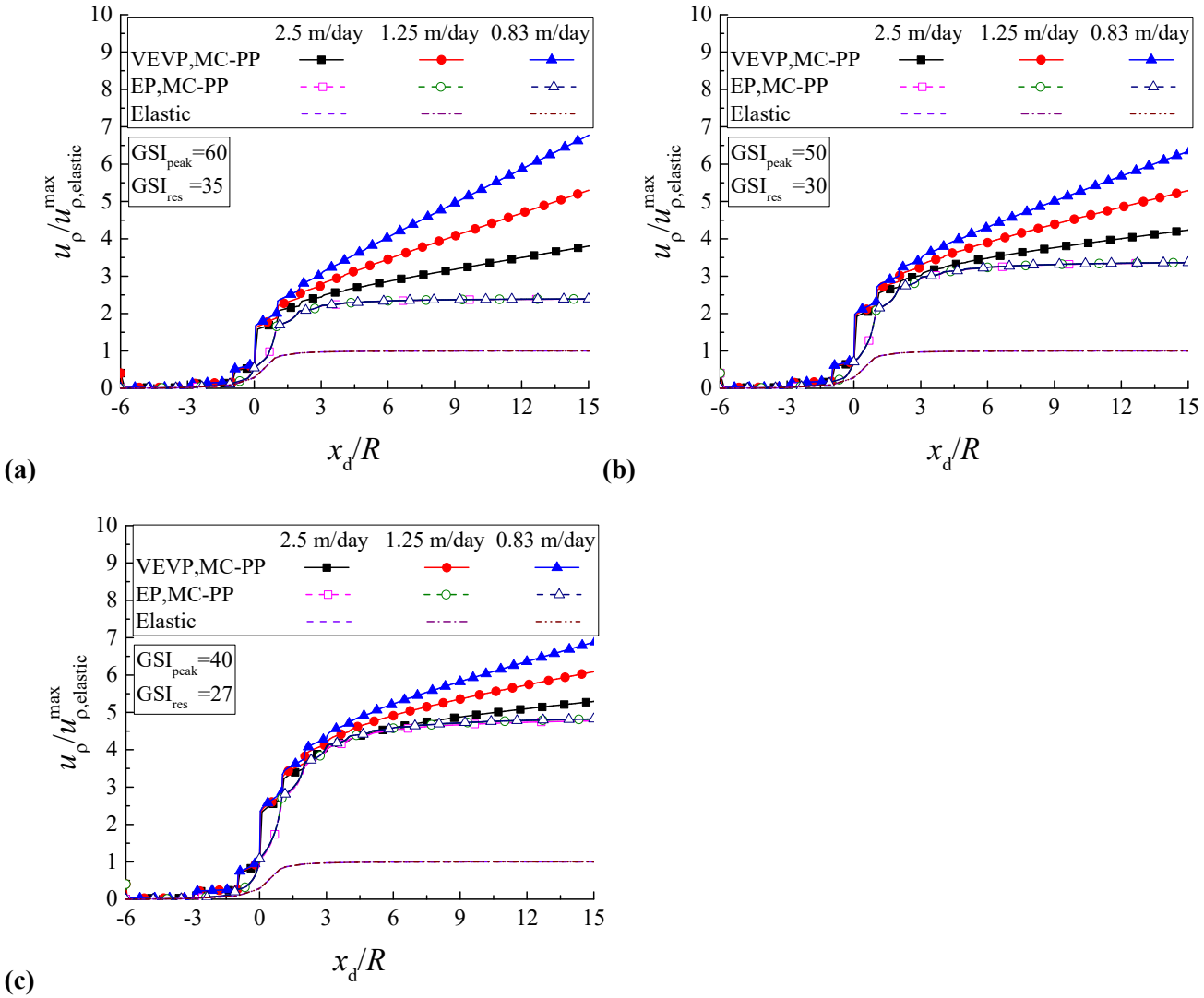

Figure 22. Normalized longitudinal deformation profiles along the normalized distance to the tunnel face for three different excavation rates (0.83 m/day, 1.25 m/day and 2.5 m/day) and for three different rock qualities: (a) GSI_{peak}=60, GSI_{res}=35, (b) GSI_{peak}=50, GSI_{res}=30, and (c) GSI_{peak}=40, GSI_{res}=27. Three different rock mass behaviour models are adopted: elastic model; the elastic-plastic and Mohr-Coulomb perfectly plastic (EP, MC-PP) model; and the viscoelastic-viscoplastic and Mohr-Coulomb perfectly plastic (VEVP, MC-PP) model.

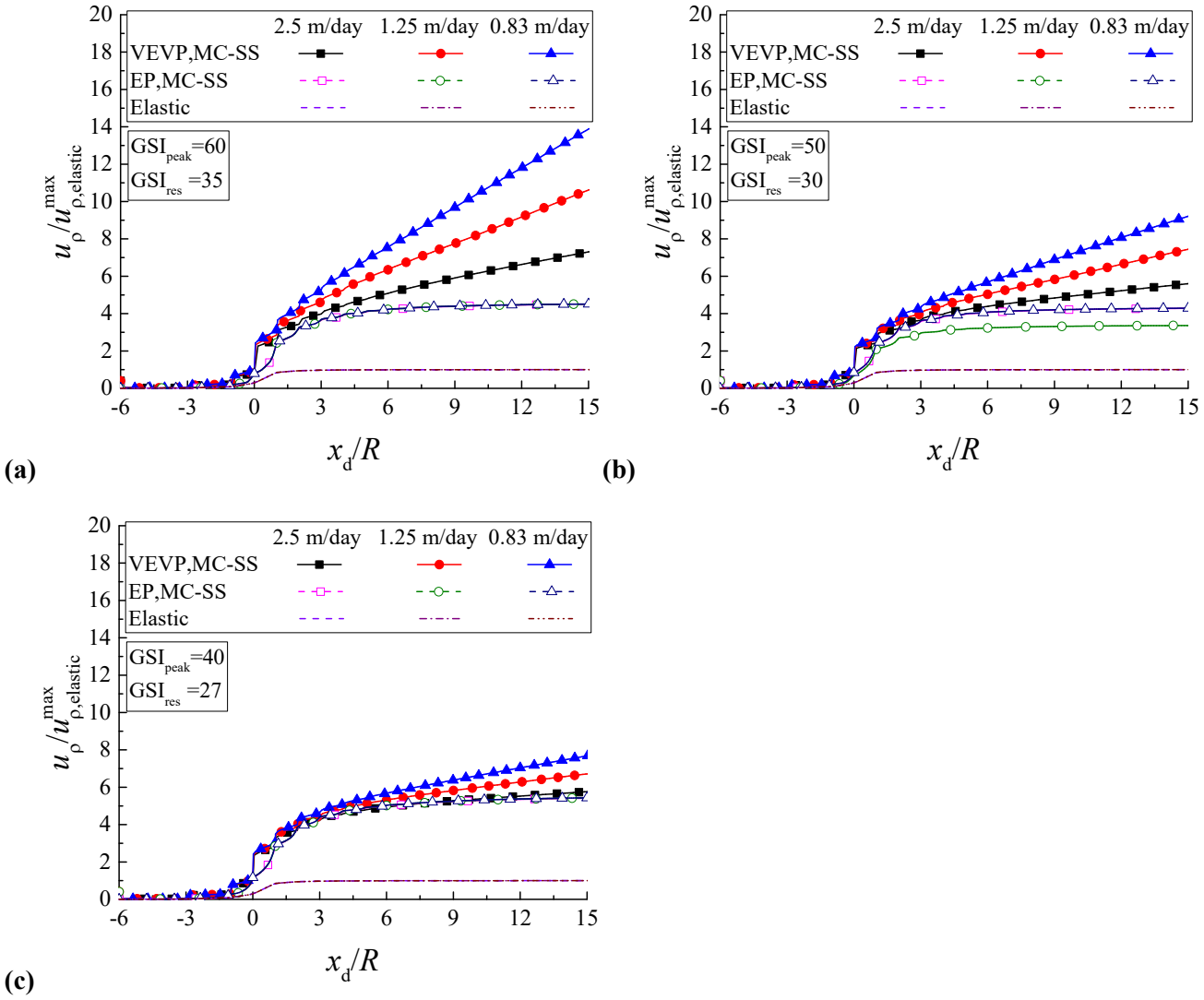

Figure 23. Normalized longitudinal deformation profiles along the normalized distance to the tunnel face for three different excavation rates (0.83 m/day, 1.25 m/day and 2.5 m/day) and for three different rock qualities: (a) GSI_{peak}=60, GSI_{res}=35, (b) GSI_{peak}=50, GSI_{res}=30, (c) GSI_{peak}=40, GSI_{res}=27. Three different rock mass behaviour models are adopted: the elastic model; the elastic-plastic and Mohr-Coulomb strain-softening (EP, MC-SS) model; and the viscoelastic-viscoplastic and Mohr-Coulomb strain-softening (VEVP, MC-SS) model.

5.3. Influence of the viscosity

As shown in Figure 5, the viscoelastic-viscoplastic model can be simplified to an elastic-viscoplastic model by assigning a sufficiently large value to η_c, while it can be simplified to a viscoelastic-plastic model when η_{vp} is close to zero. To analyse the effect of viscosity, including the viscosity of the viscous (creep) model η_c^d and the viscosity of the viscoplastic model η_{vp}, on the resulting longitudinal deformation profile (LDP), an example is presented herein. In this numerical simulation, three different excavation rates are considered: V = 0.83 m/day, V = 1.25 m/day and V = 2.5 m/day. In this sub-section, the proposed VEVP-SS model is adopted, and the post-failure behaviour is described by the Mohr-Coulomb strain-softening (MC-SS) model. It should be noted that some of the values of η_c^d and η_{vp} in this sub-section may be not realistic but are useful to perform a sensitivity analysis of viscosity.

Figure 24 shows a sensitivity analysis of the viscosity on the viscous (creep) part, η_c^d. Three different viscosities are adopted for the viscous model, $\eta_c^d = 10^{10}$ MP s, 5×10^{10} MP s, and 10^{11} MP s, and the viscosity of the viscoplastic model is adopted as $\eta_{vp} = 10^2$ MPa^{5}s. The larger the value of η_c^d is, the smaller the displacement. Figure 25 shows a sensitivity analysis of the viscosity on the viscoplastic part, η_{vp}. Three different viscosities are considered for the viscoplastic model, $\eta_{vp} = 10^2$ MPa^{5}s, 10^5 MPa^{5}s, and 10^8 MPa^{5}s, and the viscosity of the viscous model is adopted as $\eta_c^d = 10^{11}$ MPa s in this case. The smaller the value of η_{vp} is, the larger the displacement. In both Figures 24 and 25, lower excavation rates produce larger displacements, caused by larger creep displacements during the excavation process.

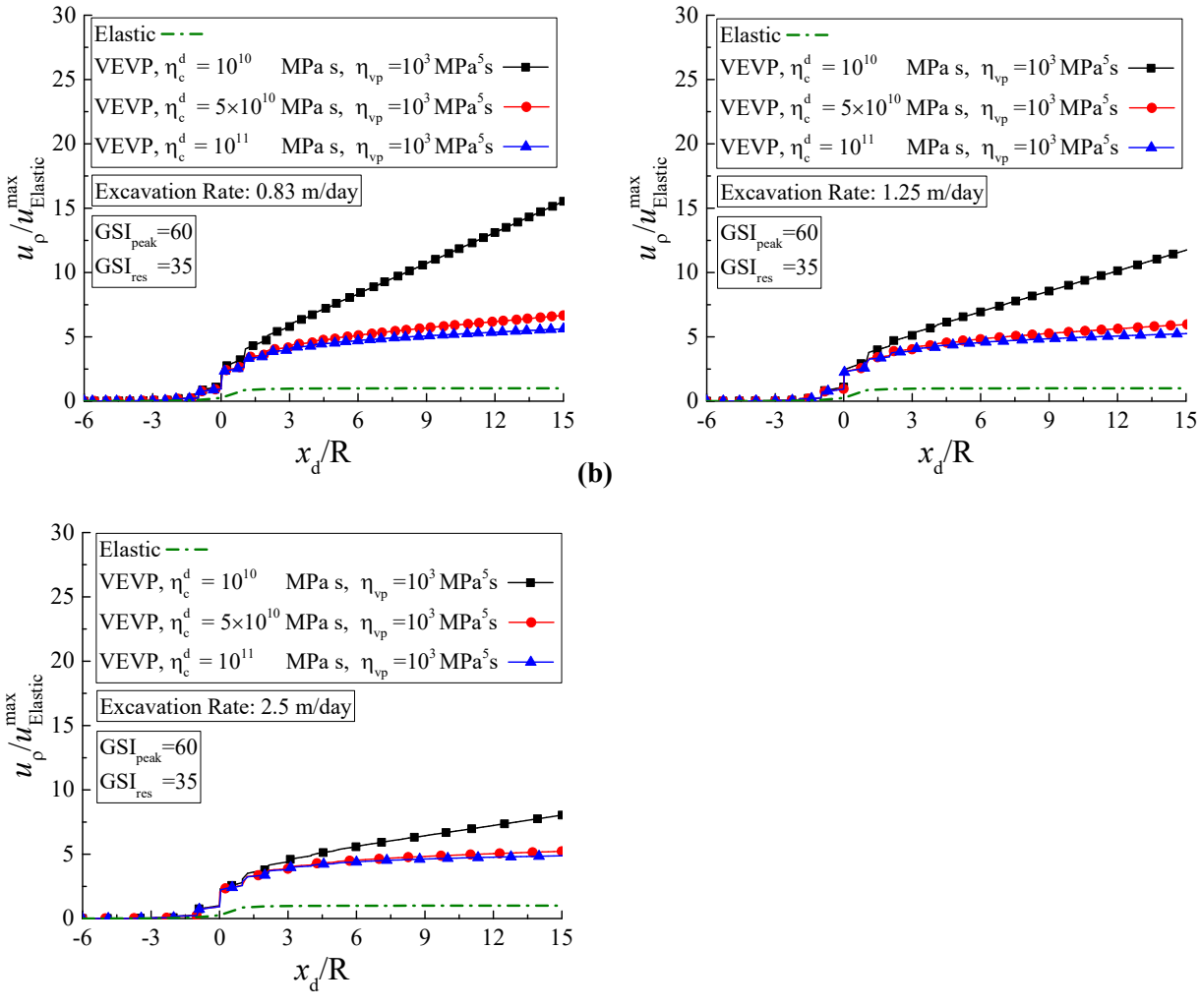

Figure 24. Normalized longitudinal deformation profiles along the normalized distance to the tunnel face by using the Mohr-Coulomb strain-softening (MC-SS) rock mass behaviour model for three different viscosities of the viscous model η_c^d, for three different excavation rates: (a) 0.83 m/day, (b) 1.25 m/day, and (c) 2.5 m/day.

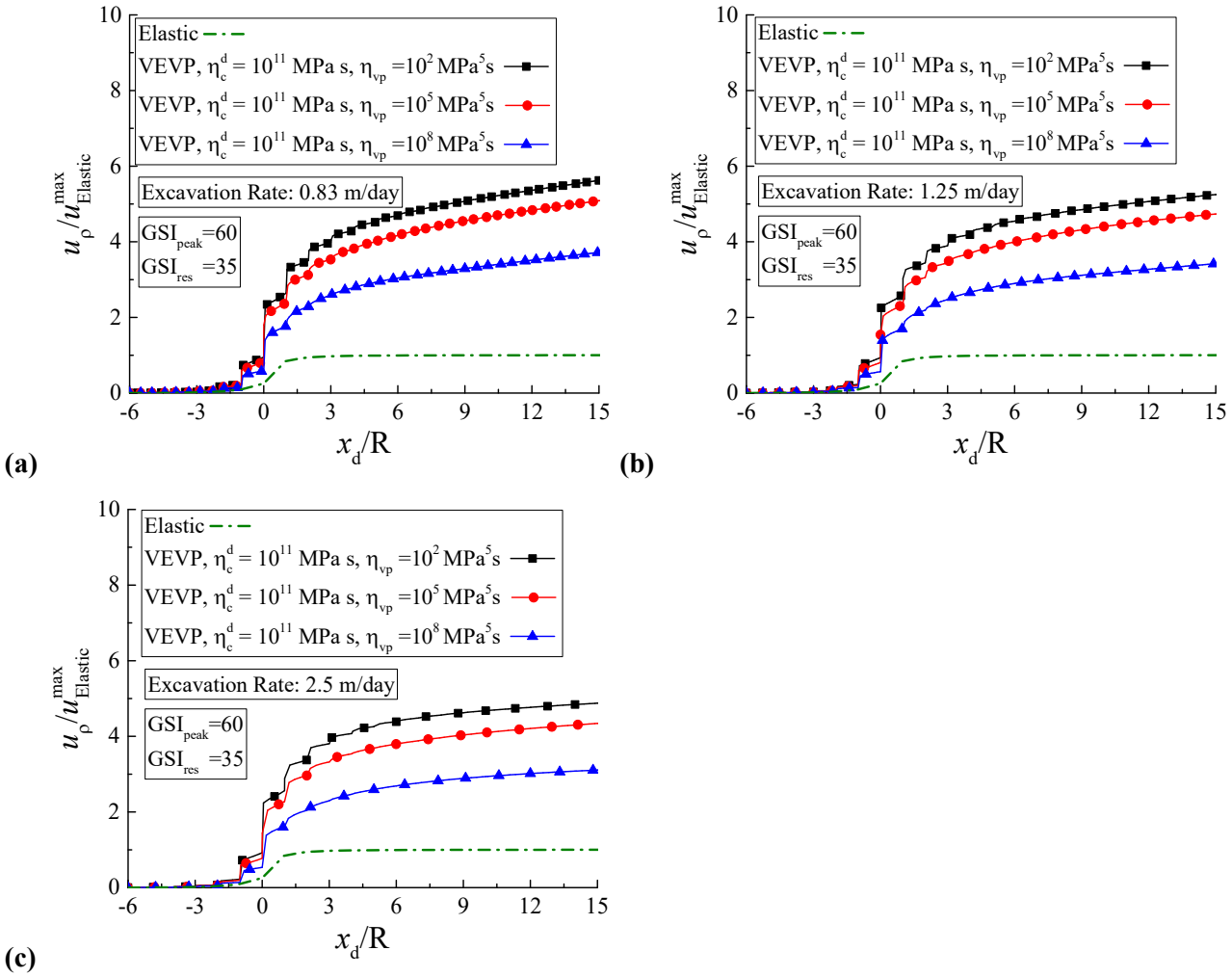

Figure 25. Normalized longitudinal deformation profiles along the normalized distance to the tunnel face by using the Mohr-Coulomb strain-softening (MC-SS) rock mass behaviour model for three different viscosities of the viscoplastic model η_{vp} and for three different excavation rates: (a) 0.83 m/day, (b) 1.25 m/day, and (c) 2.5 m/day.

6. Conclusions

This paper provides a general coupled ViscoElastic-ViscoPlastic Strain-Softening (VEVP-SS) model. This VEVP-SS model has been implemented into the finite element method software CODE_BRIGHT. In the VEVP-SS model, creep behaviour and strain-softening models are coupled, which can be used to simulate the creep-induced failure and subsequent damage of rock masses.

The viscous dashpot and the Perzyna models are adopted to simulate the creep and viscoplastic behaviours of rock masses, respectively. Both the Mohr-Coulomb and Hoek-Brown failure criteria, as well as the strain-softening post-failure behaviour of rock masses, are considered. By using a smoothing approximation method, the yield surfaces and the potential are smoothed in the numerical implementation. The numerical model is verified by a comparison between the CODE_BRIGHT results and other analytical or numerical results.

Finally, an example is carried out to predict the longitudinal deformation profile (LDP) used in the convergence-confinement method (CCM). The effects of the rock mass behaviour model selection, the geotechnical quality of the rock mass, the viscosity, and the excavation rates on the longitudinal deformation profile (LDP) are investigated. The proposed approach can be used in the preliminary design of tunnels excavated in time-dependent strain-softening rock masses. Some conclusions can be obtained from the parametric analysis:

(1) Elastic-plastic, elastic-viscoplastic, viscoelastic, viscoelastic-plastic models can be considered special cases of the VEVP-SS model, so they can be modelled using the proposed model. In addition, strain-softening post-failure behaviour or a simpler perfectly plastic or purely brittle post-failure behaviour can be selected for any case.

(2) The LDP varies according to the selected rock mass behaviour model. For instance, the displacement results of the VEVP model are larger than the corresponding elastic-plastic results due to the

contribution of the viscous (creep) behaviour. In addition, the results of the elastic and elastic-plastic models are identical for different excavation rates, while the excavation rate becomes relevant when taking into account time-dependent behaviour.

(3) When using the VEVP model, the obtained LDP obeying the Hoek-Brown failure criterion is, from an engineering point of view, similar to the obtained LDP obeying the Mohr-Coulomb failure criterion. Moreover, the difference between the LDPs calculated for perfectly plastic rock masses and for strain-softening rock masses grows as the GSI increases. Furthermore, when choosing the viscoelastic-viscoplastic rock mass behaviour model, the model is more sensitive to the excavation rate in comparison to the sensitivity of the elastic-plastic behaviour model.

(4) The proposed VEVP model is very sensitive to the input values of viscosity. For the VEVP model, the greater the values of η_c or η_{vp} are, the smaller the displacements.

Even if the proposed model can reproduce many different rock mass behaviours, there are still some limitations in the proposed VEVP-SS model. For instance, the strain rate is constant under a constant stress in the Maxwell viscoelastic model, which may reproduce only a limited number of practical cases. In future research, the Burgers viscoelastic model could be coupled with the Perzyna model to consider the influence of primary creep and thus improve the applicability of the numerical approach to real engineering.

Conflict of interest

None

Acknowledgements

The first author was supported by a UPC BarcelonaTech/CSC Joint Scholarship (No. 201706260240). This research was partially supported by the International Scientific and Technological Cooperation Projects of Shaoxing University (No. 2019LGGH1008) and the CODE_BRIGHT Project (International Centre for Numerical Methods in Engineering).

Appendix A. A smooth approximation of the Hoek-Brown failure criterion

The smooth approximation of the Hoek-Brown yield surface is derived in this appendix. The expression of the smoothed Hoke-Brown yield surface can be expressed in Eq. (19), and an alternative form of $K_{\mathrm{HB}}(\theta)$ in the vicinity of the singularities is defined for smoothing, as shown in Eq. (20). The derivatives of $K_{\mathrm{HB}}(\theta)$ with respect to θ are shown in Eq. (21).

$$F_{\mathrm{HB}} = K_{\mathrm{HB}}\left(\theta,\eta\right)\sqrt{J_2} - m_{\mathrm{HB}}\left(\eta\right)\left[-p + \frac{s_{\mathrm{HB}}\left(\eta\right)\sigma_{\mathrm{ci}}}{m_{\mathrm{HB}}\left(\eta\right)}\right] \tag{19}$$

$$K_{\mathrm{HB}}\left(\theta,\eta\right) = \begin{cases} \mathrm{A}_{\mathrm{HB}} + \mathrm{B}_{\mathrm{HB}}\sin 3\theta, & \theta \geq \left|\theta_{\mathrm{T}}\right| \\ \dfrac{4}{\sigma_{\mathrm{ci}}}\cos^2\theta\sqrt{J_2} + \dfrac{2}{\sqrt{3}}\cdot m_{\mathrm{HB}}\left(\eta\right)\cos\left(\theta + \dfrac{\pi}{6}\right), & \theta \leq \left|\theta_{\mathrm{T}}\right| \end{cases} \tag{20}$$

$$\frac{dK_{\mathrm{HB}}\left(\theta\right)}{d\theta} = \begin{cases} 3\,\mathrm{B}_{\mathrm{HB}}\cos 3\theta, & \theta \geq \left|\theta_{\mathrm{T}}\right| \\ -\dfrac{8}{\sigma_{\mathrm{ci}}}\cos\theta\sin\theta\sqrt{J_2} - \dfrac{2}{\sqrt{3}}m_{\mathrm{HB}}\left(\eta\right)\sin\left(\theta + \dfrac{\pi}{6}\right), & \theta \leq \left|\theta_{\mathrm{T}}\right| \end{cases} \tag{21}$$

The expressions of A_{HB} and B_{HB} can be obtained by matching the zero and first derivatives for the smoothed surface to those of the Hoek-Brown yield surface at θ_{T}, providing two linear equations, as shown in Eqs. (22) and (23).

$$\mathrm{A}_{\mathrm{HB}} + \mathrm{B}_{\mathrm{HB}}\sin 3\theta_{\mathrm{T}} = \frac{4}{\sigma_{\mathrm{ci}}}\cos^2\theta_{\mathrm{T}}\sqrt{J_2} + \frac{2}{\sqrt{3}}m_{\mathrm{HB}}\left(\eta\right)\cos\left(\theta_{\mathrm{T}} + \frac{\pi}{6}\right) \tag{22}$$

$$3\mathrm{B}_{\mathrm{HB}}\cos 3\theta_{\mathrm{T}} = -\frac{8}{\sigma_{\mathrm{ci}}}\cos\theta_{\mathrm{T}}\sin\theta\sqrt{J_2} - \frac{2}{\sqrt{3}}m_{\mathrm{HB}}\left(\eta\right)\sin\left(\theta_{\mathrm{T}} + \frac{\pi}{6}\right) \tag{23}$$

Finally, the coefficients of A_{HB} and B_{HB} can be determined, and the corresponding expressions are shown in Eqs. (24) and (25).

$$A_{HB} = m_{HB}(\eta)\left[\left(\cos\theta_T - \frac{\langle\theta\rangle\sin\theta_T}{\sqrt{3}}\right) + \left(\frac{\cos\theta_T}{3\sqrt{3}} + \frac{1}{3}\langle\theta\rangle\sin\theta_T\right)\langle\theta\rangle\tan 3\theta_T\right] + \sqrt{J_2}\left[\frac{4\cos^2\theta_T}{\sigma_{ci}} + \frac{8\sin\theta_T\cos\theta_T\tan 3\theta_T}{3\sigma_{ci}}\right] \quad (24)$$

$$B_{HB} = \sqrt{J_2}\left[-\frac{8\langle\theta\rangle\sin\theta_T\cos\theta_T}{3\sigma_{ci}\cos 3\theta_T}\right] - \frac{m_{HB}(\eta)}{3\cos 3\theta_T}\left[\langle\theta\rangle\sin\theta_T + \frac{\cos\theta_T}{\sqrt{3}}\right] \quad (25)$$

Figure A.1 presents the conceptual model of the smoothed Hoek-Brown yield surface in the octahedral plane.

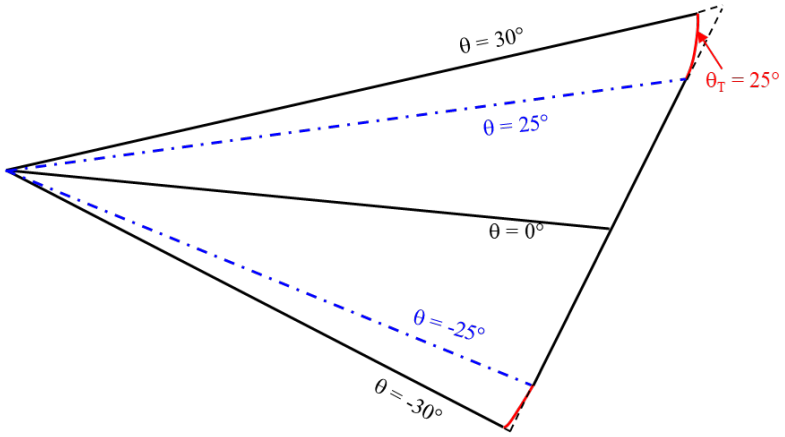

Figure A.1. The smoothed Hoek-Brown yield surface in the octahedral plane.

Appendix B. The gradients of the yield surface and potential

The gradients of the yield surface and the potential function with respect to the stresses play an essential role in the numerical implementation. The derivative of Eq. (1) with respect to the stress tensor can be expressed in Eq. (26), where the first derivative of the yield surface with respect to the stress, $\frac{\partial F}{\partial \boldsymbol{\sigma}}$, is expressed in Eq. (27); the first derivaive of the potential with respect to the stress, $\frac{\partial G}{\partial \boldsymbol{\sigma}}$, is expressed in Eq. (28); and the second derivative of the potential with respect to the stress, $\frac{\partial^2 G}{\partial \boldsymbol{\sigma}^2}$, is expressed in Eq. (29).

$$\begin{aligned}\frac{d}{d\boldsymbol{\sigma}}\left(\frac{d\boldsymbol{\varepsilon}(t)}{dt}\right)=&\frac{1}{3K_{\mathrm{M}}}\frac{d}{d\boldsymbol{\sigma}}\left(\frac{dp}{dt}\mathbf{m}\right)+\frac{1}{2G_{\mathrm{M}}}\frac{d}{d\boldsymbol{\sigma}}\left(\frac{d\boldsymbol{\sigma}}{dt}-\frac{dp}{dt}\mathbf{m}\right)+\\&\frac{1}{2\eta_{\mathrm{c}}^{\mathrm{d}}}\frac{d(\boldsymbol{\sigma}-\mathrm{p}\,\mathbf{m})}{d\boldsymbol{\sigma}}+\frac{1}{\eta_{\mathrm{vp}}}\mathrm{m}\left\langle F^{\mathrm{m\text{-}1}}\right\rangle\frac{\partial F}{\partial\boldsymbol{\sigma}}\frac{\partial G}{\partial\boldsymbol{\sigma}}+\frac{1}{\eta_{\mathrm{vp}}}\left\langle F^{\mathrm{m}}\right\rangle\frac{\partial^2 G}{\partial\boldsymbol{\sigma}^2}\end{aligned}\tag{26}$$

$$\frac{\partial F}{\partial\boldsymbol{\sigma}}=\frac{\partial F}{\partial p}\frac{\partial p}{\partial\boldsymbol{\sigma}}+\frac{\partial F}{\partial\sqrt{J_2}}\frac{\partial\sqrt{J_2}}{\partial\boldsymbol{\sigma}}+\frac{\partial F}{\partial\theta}\frac{\partial\theta}{\partial\boldsymbol{\sigma}}\tag{27}$$

$$\frac{\partial G}{\partial\boldsymbol{\sigma}}=\frac{\partial G}{\partial p}\frac{\partial p}{\partial\boldsymbol{\sigma}}+\frac{\partial G}{\partial\sqrt{J_2}}\frac{\partial\sqrt{J_2}}{\partial\boldsymbol{\sigma}}+\frac{\partial G}{\partial\theta}\frac{\partial\theta}{\partial\boldsymbol{\sigma}}\tag{28}$$

$$\begin{aligned}\frac{\partial^2 G}{\partial\boldsymbol{\sigma}^2}=&\left(\frac{\partial^2 G}{\partial\sqrt{J_2}^{\,2}}\frac{\partial\sqrt{J_2}}{\partial\boldsymbol{\sigma}}+\frac{\partial^2 G}{\partial\sqrt{J_2}\,\partial\theta}\frac{\partial\theta}{\partial\boldsymbol{\sigma}}\right)\frac{\partial\sqrt{J_2}}{\partial\boldsymbol{\sigma}}+\frac{\partial G}{\partial\sqrt{J_2}}\frac{\partial^2\sqrt{J_2}}{\partial\boldsymbol{\sigma}^2}\\&+\left(\frac{\partial^2 G}{\partial\theta\,\partial\sqrt{J_2}}\frac{\partial\sqrt{J_2}}{\partial\boldsymbol{\sigma}}+\frac{\partial^2 G}{\partial\theta^2}\frac{\partial\theta}{\partial\boldsymbol{\sigma}}\right)\frac{\partial\theta}{\partial\boldsymbol{\sigma}}+\frac{\partial G}{\partial\theta}\frac{\partial^2\theta}{\partial\boldsymbol{\sigma}^2}\end{aligned}\tag{29}$$

Appendix B.1 and appendix B.2 present the first derivative expressions of the failure criteria and the first and second derivative expressions of the potential, respectively.

Appendix B.1. The first derivative expressions of the Mohr-Coulomb and Hoek-Brown failure criteria

The first derivative of the failure surface is shown in Eq. (30).

$$\frac{\partial F}{\partial \boldsymbol{\sigma}} = \frac{\partial F}{\partial p}\frac{\partial p}{\partial \boldsymbol{\sigma}} + \frac{\partial F}{\partial \sqrt{J_2}}\frac{\partial \sqrt{J_2}}{\partial \boldsymbol{\sigma}} + \frac{\partial F}{\partial \theta}\frac{\partial \theta}{\partial \boldsymbol{\sigma}} \tag{30}$$

For the Mohr-Coulomb failure criterion,

$$\frac{\partial F_{\mathrm{MC}}}{\partial p} = \sin\varphi \tag{31}$$

$$\frac{\partial F_{\mathrm{MC}}}{\partial \sqrt{J_2}} = \frac{K_{\mathrm{MC}}^2\sqrt{J_2}}{\sqrt{J_2 K_{\mathrm{MC}}^2 + a^2\sin^2\varphi}} \tag{32}$$

$$\frac{\partial F_{\mathrm{MC}}}{\partial \theta} = \frac{J_2 K_{\mathrm{MC}}}{\sqrt{J_2 K_{\mathrm{MC}}^2 + a^2\sin^2\varphi}}\frac{dK_{\mathrm{MC}}}{d\theta} \tag{33}$$

where

$$\frac{dK_{\mathrm{MC}}(\theta,\eta)}{d\theta} = \begin{cases} 3B_{\mathrm{MC}}\cos 3\theta, & |\theta| > \theta_{\mathrm{T}} \\ -\sin\theta - \dfrac{1}{\sqrt{3}}\sin\varphi(\eta)\cos\theta, & |\theta| \le \theta_{\mathrm{T}} \end{cases} \tag{34}$$

For the Hoek-Brown failure criterion,

$$\frac{\partial F_{\mathrm{HB}}}{\partial p} = m_{\mathrm{HB}}(\eta) \tag{35}$$

$$\frac{\partial F_{\mathrm{HB}}}{\partial \sqrt{J_2}} = \frac{dK_{\mathrm{HB}}(\theta,\eta)}{d\sqrt{J_2}}\sqrt{J_2} + K_{\mathrm{HB}}(\theta,\eta) \tag{36}$$

$$\frac{\partial F_{\mathrm{HB}}}{\partial \theta} = \frac{dK_{\mathrm{HB}}(\theta,\eta)}{d\theta}\sqrt{J_2} \tag{37}$$

where

$$\frac{dK_{\mathrm{HB}}(\theta,\eta)}{d\sqrt{J_2}}=\begin{cases}\dfrac{dA_{\mathrm{HB}}}{d\sqrt{J_2}}+\dfrac{dB_{\mathrm{HB}}}{d\sqrt{J_2}}\sin 3\theta, & \theta>\left|\theta_{\mathrm{T}}\right| \\ \dfrac{4}{\sigma_{\mathrm{ci}}}\cos^2\theta, & \theta\le\left|\theta_{\mathrm{T}}\right|\end{cases} \tag{38}$$

$$\frac{dK_{\mathrm{HB}}(\theta,\eta)}{d\theta}=\begin{cases}3B_{\mathrm{HB}}\cos 3\theta, & \theta>\left|\theta_{\mathrm{T}}\right| \\ -\dfrac{8}{\sigma_{\mathrm{ci}}}\cos\theta\sin\theta\sqrt{J_2}-\dfrac{2}{\sqrt{3}}m_{\mathrm{HB}}(\eta)\sin\left(\theta+\dfrac{\pi}{6}\right), & \theta\le\left|\theta_{\mathrm{T}}\right|\end{cases} \tag{39}$$

$$\frac{dA_{\mathrm{HB}}}{d\sqrt{J_2}}=\frac{4\cos^2\theta_{\mathrm{T}}}{\sigma_{\mathrm{ci}}}+\frac{8\sin\theta_{\mathrm{T}}\cos\theta_{\mathrm{T}}\tan 3\theta_{\mathrm{T}}}{3\sigma_{\mathrm{ci}}} \tag{40}$$

$$\frac{dB_{\mathrm{HB}}}{d\sqrt{J_2}}=-\frac{8\langle\theta\rangle\sin\theta_{\mathrm{T}}\cos\theta_{\mathrm{T}}}{3\sigma_{\mathrm{ci}}\cos 3\theta_{\mathrm{T}}} \tag{41}$$

Appendix B.2. The first and second derivative expressions of the potential function

The first derivative of the potential function is presented in Eq. (42).

$$\frac{\partial G}{\partial\boldsymbol{\sigma}}=\frac{\partial G}{\partial p}\frac{\partial p}{\partial\boldsymbol{\sigma}}+\frac{\partial G}{\partial\sqrt{J_2}}\frac{\partial\sqrt{J_2}}{\partial\boldsymbol{\sigma}}+\frac{\partial G}{\partial\theta}\frac{\partial\theta}{\partial\boldsymbol{\sigma}} \tag{42}$$

where

$$\frac{\partial G}{\partial p}=\alpha\sin\psi \tag{43}$$

$$\frac{\partial G}{\partial\sqrt{J_2}}=2K_{\mathrm{G}}^2(\theta)\sqrt{J_2} \tag{44}$$

$$\frac{\partial G}{\partial\theta}=2J_2K_{\mathrm{G}}\frac{dK_{\mathrm{G}}}{d\theta} \tag{45}$$

$$\frac{dK_{\mathrm{G}}(\theta)}{d\theta}=\begin{cases}3E_{\mathrm{G}}\cos 3\theta+6F_{\mathrm{G}}\sin 3\theta\cos 3\theta, & |\theta|>\theta_{\mathrm{T}}\\ -\sin\theta-\dfrac{1}{\sqrt{3}}\sin\psi\cos\theta, & |\theta|\le\theta_{\mathrm{T}}\end{cases} \tag{46}$$

The second derivative of plastic potential function is presented in Eq. (47).

$$\begin{aligned}\frac{\partial^2 G}{\partial\boldsymbol{\sigma}^2}=&\left(\frac{\partial^2 G}{\partial\sqrt{J_2}^2}\frac{\partial\sqrt{J_2}}{\partial\boldsymbol{\sigma}}+\frac{\partial^2 G}{\partial\sqrt{J_2}\partial\theta}\frac{\partial\theta}{\partial\boldsymbol{\sigma}}\right)\frac{\partial\sqrt{J_2}}{\partial\boldsymbol{\sigma}}+\frac{\partial G}{\partial\sqrt{J_2}}\frac{\partial^2\sqrt{J_2}}{\partial\boldsymbol{\sigma}^2}\\&+\left(\frac{\partial^2 G}{\partial\theta\partial\sqrt{J_2}}\frac{\partial\sqrt{J_2}}{\partial\boldsymbol{\sigma}}+\frac{\partial^2 G}{\partial\theta^2}\frac{\partial\theta}{\partial\boldsymbol{\sigma}}\right)\frac{\partial\theta}{\partial\boldsymbol{\sigma}}+\frac{\partial G}{\partial\theta}\frac{\partial^2\theta}{\partial\boldsymbol{\sigma}^2}\end{aligned} \tag{47}$$

where

$$\frac{\partial^2 G}{\partial\sqrt{J_2}^2}=2K_{\mathrm{G}}^2(\theta) \tag{48}$$

$$\frac{\partial^2 G}{\partial\sqrt{J_2}\partial\theta}=\frac{\partial^2 G}{\partial\theta\partial\sqrt{J_2}}=4K_{\mathrm{G}}(\theta)\sqrt{J_2}\frac{dK_{\mathrm{G}}(\theta)}{d\theta} \tag{49}$$

$$\frac{\partial^2 G}{\partial\theta^2}=2J_2\frac{dK_{\mathrm{G}}}{d\theta}\frac{dK_{\mathrm{G}}}{d\theta}+2J_2K_{\mathrm{G}}\frac{d^2K_{\mathrm{G}}}{d\theta^2} \tag{50}$$

$$\frac{d^2K_{\mathrm{G}}(\theta)}{d\theta^2}=\begin{cases}-9E_{\mathrm{G}}\sin 3\theta+18F_{\mathrm{G}}\cos 6\theta, & |\theta|>\theta_{\mathrm{T}}\\ -\cos\theta+\dfrac{1}{\sqrt{3}}\sin\psi\sin\theta, & |\theta|\le\theta_{\mathrm{T}}\end{cases} \tag{51}$$

References

[1] Zhao K, Bonini M, Debernardi D, Janutolo M, Barla G, Chen G. Computational modelling of the mechanised excavation of deep tunnels in weak rock. Computers and Geotechnics. 2015;66:158-171.

[2] Zhou ZL, Cai X, Li XB, Cao WZ, Du XM. Dynamic response and energy evolution of sandstone under coupled static–dynamic compression: insights from experimental study into deep rock engineering applications. Rock Mechanics and Rock Engineering. 2019:1-27.

[3] Fabre G, Pellet F. Creep and time-dependent damage in argillaceous rocks. International Journal of Rock Mechanics and Mining Sciences. 2006;43(6):950-960.

[4] Eberhardt E, Stimpson B, Stead D. The influence of mineralogy on the initiation of microfractures in granite. 9th ISRM Congress, 1999.

[5] Damjanac B, Fairhurst C. Evidence for a long-term strength threshold in crystalline rock. Rock Mechanics and Rock Engineering. 2010;43(5):513-531.

[6] Barla G, Borgna S. Numerical modelling of squeezing behaviour in tunnels. 2000.

[7] Paraskevopoulou C. Time-dependency of rocks and implications associated with tunnelling. 2016.

[8] Wang HN, Nie GH. Analytical expressions for stress and displacement fields in viscoelastic axisymmetric plane problem involving time-dependent boundary regions. Acta mechanica. 2010;210(3-4):315-330.

[9] Song F, Wang HN, Jiang MJ. Analytical solutions for lined circular tunnels in viscoelastic rock considering various interface conditions. Applied Mathematical Modelling. 2018;55:109-130.

[10] Wang HN, Zeng GS, Jiang MJ. Analytical stress and displacement around non-circular tunnels in semi-infinite ground. Applied Mathematical Modelling. 2018;63:303-328.

[11] Conte E, Donato A, Troncone A. Progressive failure analysis of shallow foundations on soils with strain-softening behaviour. Computers and Geotechnics. 2013;54:117-124.

[12] Deng PH, Liu QS. Influence of the softening stress path on crack development around underground excavations: Insights from 2D-FDEM modelling. Computers and Geotechnics. 2020;117:103239.

[13] Doležalová M. Tunnel complex unloaded by a deep excavation. Computers and Geotechnics. 2001;28(6-7):469-493.

[14] Galli G, Grimaldi A, Leonardi A. Three-dimensional modelling of tunnel excavation and lining. Computers and Geotechnics. 2004;31(3):171-183.

[15] Sainoki A, Tabata S, Mitri HS, Fukuda D, Kodama J-i. Time-dependent tunnel deformations in homogeneous and heterogeneous weak rock formations. Computers and Geotechnics. 2017;92:186-200.

[16] Wang HN, Gao X, Wu L, Jiang MJ. Analytical study on interaction between existing and new tunnels parallel excavated in semi-infinite viscoelastic ground. Computers and Geotechnics. 2020;120:103385.

[17] Wang HN, Gong H, Liu F, Jiang MJ. Size-dependent mechanical behavior of an intergranular bond revealed by an analytical model. Computers and Geotechnics. 2017;89:153-167.

[18] Zhang Q, Wang HY, Jiang YJ, Lu MM, Jiang BS. A numerical large strain solution for circular tunnels excavated in strain-softening rock masses. Computers and Geotechnics. 2019;114:103142.

[19] Zhu HH, Ye B, Cai YC, Zhang F. An elasto-viscoplastic model for soft rock around tunnels considering overconsolidation and structure effects. Computers and Geotechnics. 2013;50:6-16.

[20] Zou JF, Li C, Wang F. A new procedure for ground response curve (GRC) in strain-softening surrounding rock. Computers and Geotechnics. 2017;89:81-91.

[21] Song F, Wang HN, Jiang MJ. Analytically-based simplified formulas for circular tunnels with two liners in viscoelastic rock under anisotropic initial stresses. Construction and Building Materials. 2018;175:746-767.

[22] Manica M. Analysis of underground excavations in argillaceous hard soils - weak rocks [Ph.D. Thesis]. Barcelona. Technical University of Catalonia, 2018.

[23] Paraskevopoulou C, Perras M, Diederichs M, Loew S, Lam T, Jensen M. Time-Dependent Behaviour of Brittle Rocks Based on Static Load Laboratory Tests. Geotechnical and Geological Engineering. 2018;36(1):337-376.

[24] Alonso E, Alejano LR, Varas F, Fdez-Manin G, Carranza-Torres C. Ground response curves for rock masses exhibiting strain-softening behaviour. International journal for numerical and analytical methods in geomechanics. 2003;27(13):1153-1185.

[25] Barla G, Debernardi D, Sterpi D. Time-dependent modeling of tunnels in squeezing conditions. International Journal of Geomechanics. 2011;12(6):697-710.

[26] Alejano LR, Alonso E, Rodriguez-Dono A, Fernandez-Manin G. Application of the convergence-confinement method to tunnels in rock masses exhibiting Hoek–Brown strain-softening behaviour. International Journal of Rock Mechanics and Mining Sciences. 2010;1(47):150-160.

[27] Carranza-Torres C, Fairhurst C. The elasto-plastic response of underground excavations in rock masses that satisfy the Hoek–Brown failure criterion. International Journal of Rock Mechanics and Mining Sciences. 1999;36(6):777-809.

[28] Cui L, Sheng Q, Zheng JJ, Cui Z, Wang A, Shen Q. Regression model for predicting tunnel strain in strain-softening rock mass for underground openings. International Journal of Rock Mechanics and Mining Sciences. 2019;119:81-97.

[29] Cui L, Zheng JJ, Zhang RJ, Lai HJ. A numerical procedure for the fictitious support pressure in the application of the convergence–confinement method for circular tunnel design. International Journal of Rock Mechanics and Mining Sciences. 2015;78:336-349.

[30] Sulem J, Panet M, Guenot A. An analytical solution for time-dependent displacements in a circular tunnel. International journal of rock mechanics and mining sciences & geomechanics abstracts, 1987:24(3):155-164.

[31] de la Fuente M, Sulem J, Taherzadeh R, Subrin D. Tunneling in Squeezing Ground: Effect of the Excavation Method. Rock Mechanics and Rock Engineering. 2019:1-23.

[32] Vlachopoulos N, Diederichs MS. Improved longitudinal displacement profiles for convergence confinement analysis of deep tunnels. Rock mechanics and rock engineering. 2009;42(2):131-146.

[33] Wang HN, Li Y, Ni Q, Utili S, Jiang MJ, Liu F. Analytical solutions for the construction of deeply buried circular tunnels with two liners in rheological rock. Rock mechanics and rock engineering. 2013;46(6):1481-1498.

[34] Wang HN, Utili S, Jiang MJ, He P. Analytical solutions for tunnels of elliptical cross-section in rheological rock accounting for sequential excavation. Rock mechanics and rock engineering. 2015;48(5):1997-2029.

[35] Alejano LR, Rodriguez-Dono A, Alonso E, Manín GF. Ground reaction curves for tunnels excavated in different quality rock masses showing several types of post-failure behaviour. Tunnelling and Underground Space Technology. 2009;24(6):689-705.

[36] Alejano LR, Rodríguez-Dono A, Veiga M. Plastic radii and longitudinal deformation profiles of tunnels excavated in strain-softening rock masses. Tunnelling and Underground Space Technology. 2012;30:169-182.

[37] Carranza-Torres C, Fairhurst C. Application of the convergence-confinement method of tunnel design to rock masses that satisfy the Hoek-Brown failure criterion. Tunnelling and Underground Space Technology. 2000;15(2):187-213.

[38] Yi CK, Senent S, Jimenez R. Effect of advance drainage on tunnel face stability using Limit Analysis and numerical simulations. Tunnelling and Underground Space Technology. 2019;93:103105.

[39] Debernardi D, Barla G. New viscoplastic model for design analysis of tunnels in squeezing conditions. Rock mechanics and rock engineering. 2009;42(2):259.

[40] Kitagawa T, Kumeta T, Ichizyo T, Soga S, Sato M, Yasukawa M. Application of convergence confinement analysis to the study of preceding displacement of a squeezing rock tunnel. Rock mechanics and rock engineering. 1991;24(1):31-51.

[41] Paraskevopoulou C, Diederichs M. Analysis of time-dependent deformation in tunnels using the Convergence-Confinement Method. Tunnelling and Underground Space Technology. 2018;71:62-80.

[42] Sterpi D, Gioda G. Visco-plastic behaviour around advancing tunnels in squeezing rock. Rock Mechanics and Rock Engineering. 2009;42(2):319-339.

[43] Wang HN, Utili S, Jiang MJ. An analytical approach for the sequential excavation of axisymmetric lined tunnels in viscoelastic rock. International Journal of Rock Mechanics and Mining Sciences. 2014;68:85-106.

[44] Wang HN, Zeng GS, Utili S, Jiang MJ, Wu L. Analytical solutions of stresses and displacements for deeply buried twin tunnels in viscoelastic rock. International Journal of Rock Mechanics and Mining Sciences. 2017;93:13-29.

[45] Fenner R. Untersuchungen zur erkenntnis des gebirgsdrucks. Glückauf, 1938.

[46] Corbetta F, Bernaud D, Minh DN. Contribution à la méthode convergence-confinement par le principe de la similitude. Revue française de géotechnique. 1991(54):5-11.

[47] Kabwe E, Karakus M, Chanda EK. Proposed solution for the ground reaction of non-circular tunnels in an elastic-perfectly plastic rock mass. Computers and Geotechnics. 2020;119:103354.

[48] Wang SL, Yin XT, Tang H, Ge XR. A new approach for analyzing circular tunnel in strain-softening rock masses. International journal of rock mechanics and mining sciences (1997). 2010;47(1):170-178.

[49] Zhang Q, Jiang BS, Wang SL, Ge XR, Zhang HQ. Elasto-plastic analysis of a circular opening in strain-softening rock mass. International Journal of Rock Mechanics and Mining Sciences. 2012;50:38-46.

[50] Hoek E, Brown ET. Underground excavations in rock. 1980.

[51] Oreste P. Distinct analysis of fully grouted bolts around a circular tunnel considering the congruence of displacements between the bar and the rock. International Journal of Rock Mechanics and Mining Sciences. 2008;45(7):1052-1067.

[52] Oreste PP. Analysis of structural interaction in tunnels using the covergence–confinement approach. Tunnelling and Underground Space Technology. 2003;18(4):347-363.

[53] Panet M. Understanding deformations in tunnels. Comprehensive rock engineering. 1993;1:663-690.

[54] Panet M. Le calcul des tunnels par la méthode convergence-confinement. Presses ENPC, 1995.

[55] Unlu T, Gercek H. Effect of Poisson's ratio on the normalized radial displacements occurring around the face of a circular tunnel. Tunnelling and Underground Space Technology. 2003;18(5):547-553.

[56] Hoek E, Brown ET. Practical estimates of rock mass strength. International journal of rock mechanics and mining sciences. 1997;34(8):1165-1186.

[57] Malan DF. Manuel Rocha medal recipient simulating the time-dependent behaviour of excavations in hard rock. Rock Mechanics and Rock Engineering. 2002;35(4):225-254.

[58] Desai CS, Zhang D. Viscoplastic model for geologic materials with generalized flow rule. International Journal for Numerical and Analytical Methods in Geomechanics. 1987;11(6):603-620.

[59] Karim MR, Oka F, Krabbenhoft K, Leroueil S, Kimoto S. Simulation of long-term consolidation behavior of soft sensitive clay using an elasto-viscoplastic constitutive model. International Journal for Numerical and Analytical Methods in Geomechanics. 2013;37(16):2801-2824.

[60] Kutter BL, Sathialingam N. Elastic-viscoplastic modelling of the rate-dependent behaviour of clays. Géotechnique. 1992;42(3):427-441.

[61] Pellet F, Hajdu A, Deleruyelle F, Besnus F. A viscoplastic model including anisotropic damage for the time dependent behaviour of rock. International journal for numerical and analytical methods in geomechanics. 2005;29(9):941-970.

[62] Itasca. FLAC Version 7. Fast Lagrangian Analysis of Continua. 2D Version. Minneapolis, Minnesota, USA, 2011. < http://www.itascacg.com>

[63] Olivella S, Jean V, Alfonso RD. CODE_BRIGHT USER'S GUIDE. Barcelona, Spain. Division of Geotechnical Engineering and Geosciences, Department of Civil and Environmental Engineering, Technical University of Catalonia (UPC) , 2020. <https://deca.upc.edu/en/projects/code_bright>

[64] Itasca. FLAC3D Version 3. Fast Lagrangian Analysis of Continua, 3D Version. Minneapolis, Minnesota, USA, 2007. < http://www.itascacg.com>

[65] Perzyna P. Fundamental problems in viscoplasticity. Elsevier, 1966.

[66] Chu ZF, Wu ZJ, Liu BG, Liu QS. Coupled analytical solutions for deep-buried circular lined tunnels considering tunnel face advancement and soft rock rheology effects. Tunnelling and Underground Space Technology. 2019;94:103111.

[67] Tomanovic Z. Rheological model of soft rock creep based on the tests on marl. Mechanics of Time-Dependent Materials. 2006;10(2):135-154.

[68] Ramírez Oyanguren P. A study of longwall mining in potash. University of Newcastle, 1966.

[69] Günther R-M, Salzer K, Popp T, Lüdeling C. Steady-state creep of rock salt: improved approaches for lab determination and modelling. Rock Mechanics and Rock Engineering. 2015;48(6):2603-2613.

[70] Olivella S, Gens A. A constitutive model for crushed salt. International journal for numerical and analytical methods in geomechanics. 2002;26(7):719-746.

[71] Starfield AM, Cundall P. Towards a methodology for rock mechanics modelling. international journal of rock mechanics and mining sciences & geomechanics abstracts, 1988:25(3):99-106.

[72] Alonso E, Olivella S, Pinyol N. A review of Beliche Dam. Géotechnique. 2005;55(4):267-285.

[73] Lee Y-K, Pietruszczak S. A new numerical procedure for elasto-plastic analysis of a circular opening excavated in a strain-softening rock mass. Tunnelling and Underground Space Technology. 2008;23(5):588-599.

[74] Abbo AJ, Lyamin AV, Sloan SW, Hambleton JP. A C2 continuous approximation to the Mohr–Coulomb yield surface. International Journal of solids and Structures. 2011;48(21):3001-3010.

[75] Abbo AJ, Sloan SW. A smooth hyperbolic approximation to the Mohr-Coulomb yield criterion. Computers & structures. 1995;54(3):427-441.

[76] Cristescu N, Hunsche U. Time effects in rock mechanics. Wiley New York, 1998.

[77] Sandrone F, Labiouse V. Analysis of the evolution of road tunnels equilibrium conditions with a convergence–confinement approach. Rock mechanics and rock engineering. 2010;43(2):201-218.